A Search for W_{bJ} in Decays of $\Upsilon(5S)$: An Analysis Design Study

by

Nicholas Corrado

Submitted to the Graduate Faculty of

the Kenneth P. Dietrich School of Arts and Sciences in partial fulfillment

of the requirements for the degree of

Bachelor of Philosophy

University of Pittsburgh

2019

UNIVERSITY OF PITTSBURGH

DEPARTMENT OF PHYSICS AND ASTRONOMY

This thesis was presented

by

Nicholas Corrado

It was defended on

April 2nd 2019

and approved by

Dr. Vladimir Savinov, Department of Physics and Astronomy

Dr. Vittorio Paolone, Department of Physics and Astronomy

Dr. James Mueller, Department of Physics and Astronomy

Dr. Roy Briere, Department of Physics, Carnegie Mellon University

Thesis Advisor: Dr. Vladimir Savinov, Department of Physics and Astronomy

A Search for W_{bJ} in Decays of $\Upsilon(5S)$: An Analysis Design Study

Nicholas Corrado, B.Phil

University of Pittsburgh, 2019

The recent discovery of the states Z_b and Z_b' implies the possible existence of a new family of hadronic resonances including molecular states dubbed W_{bJ}. We search for W_{bJ} in the decay $\Upsilon(5S) \to \gamma W_{bJ}$ using 121.4 fb^{-1} of data collected at the Υ(5S) resonance with the Belle detector at the KEKB asymmetric-energy electron-positron collider. Using Monte Carlo simulation, we study Belle's sensitivity to the decay $\Upsilon(5S) \to \gamma W_{bJ}$ and report the current status of our analysis.

Table of Contents

List of Figures

List of Tables

1.0 Introduction

1.1 Theoretical Background

1.1.1 Motivation

In this document, we design a search for new hadronic states of matter – bottomonium-like particles dubbed W_{bJ} – in radiative decays of $\Upsilon(5S)$. These states are believed to be of molecular nature, where a pair of colored $B^{(*)}_{(s)}$ mesons, each containing a b or an anti-b quark, are held together by the strong interaction (in a way similar to single-pion exchange force mechanism in QCD-inspired low-energy models). As with conventional bottomonium, *i.e.* $b\bar{b}$ states, these molecular states exhibit their own spectroscopy. However, their masses and properties obviously could not be predicted using $q\bar{q}$ potential models. We are motivated by Belle's discoveries [1, 2, 3, 4] of the $Z_b(10610)$ and $Z_b(10650)$ states (referred to in the rest of this document as Z_b) and theoretical predictions which use the molecular picture to explain the nature of the Z_b and predict the existence of additional hadronic states. These predications can be used to explain various long-standing puzzles in the (no longer pure) bottomonium at energies above the threshold for B meson pair production.

1.1.2 A New Spectroscopy

Since the discovery of the Υ meson, the b quark, and B mesons [5], conventional bottomonium states have been a rich source of information about strong interaction dynamics in the approximately non-relativistic $b\bar{b}$ system. Vector bottomonium and bottomonium-like states ($\Upsilon(nS)$ mesons) can be produced directly in the e^+e^- annihilation. Three of these states – $\Upsilon(1S)$, $\Upsilon(2S)$, and $\Upsilon(3S)$ – have masses below the $B\bar{B}$ threshold [6]. These states are believed to be pure $b\bar{b}$, and their properties are relatively easy to understand using potential models. Such relativized models [7] predict 34 $b\bar{b}$ bound states below $\Upsilon(4S)$ energy, 15 of which have been observed. We show the predictions for the energy levels in the $b\bar{b}$ spectroscopy [8, 9] in Figure 1.

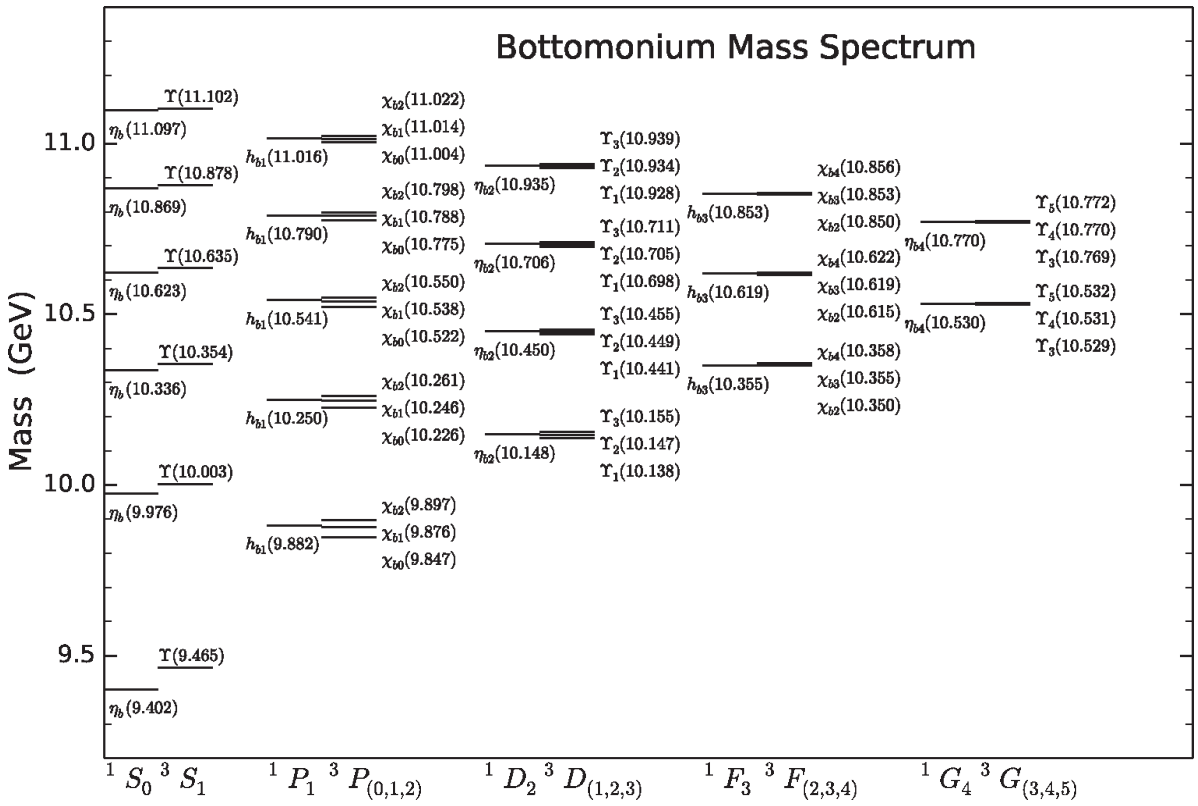

Figure 1: Pure (*i.e.* $b\bar{b}$) bottomonium mass spectrum [8] calculated using a relativized quark model [7].

Hadronic transitions (such as, *e.g.* $\Upsilon(3S) \to \pi^+\pi^-\Upsilon(1S)$) between bottomonium states provide an excellent opportunity to study QCD dynamics in non-perturbative regime by comparing the measured masses, widths, branching fractions, angular and invariant mass distributions with the theoretical predictions. For pure bottomonium states – $b\bar{b}$ resonances below $B\bar{B}$ threshold – the hadronic transitions proceed via radiating the strong field, *i.e.*, by emitting the gluons which convert into light hadrons. States above $B\bar{B}$ threshold, starting with $\Upsilon(4S)$, are significanly wider than the lower-mass states, and their hadronic transitions are known to exhibit certain properties that are unexpected for pure $b\bar{b}$ states. While the latter are well described from the perspective of Heavy Quark Spin Symmetry (HQSS) where transitions involving the spin of the heavy b quark are strongly suppressed, the former states, including the $\Upsilon(5S)$, require a different explanation [10].

The favored explanation for the properties of $\Upsilon(5S)$, including its decays to Z_b, is based

on the molecular picture, where these vector bottomonium-like resonances are assumed to contain an admixture of pairs of colored heavy mesons. This hypothesis has been successfully employed [11] to explain the decays to and the existence of the six Z_b states. However, the details of the interaction responsible for these processes are not yet fully understood. Alternative explanations include a model with a diquark-antidiquark pair, where a pair of quarks and a pair of antiquarks are each bound with a stronger force than the force holding diquark and antidiquark together. While the search described in this document is model-independent, our motivation is somewhat biased in favor of the molecular picture and has likely impacted our decisions about how to perform the analysis.

The main goal of out study is to test some of the predictions of the new spectroscopy [12] that predicts energy levels for the molecular bottomonium-like states depicted in Figure 2, Namely, we aim to design a search for the partner states of Z_b, referred to as W_{bJ}, and we aim to obtain new information about hadronic dynamics in presence of the heavy b quarks. Improving the current understanding of such dynamics is of paramount importance for being able to use the hadronic decays of B mesons to extract possible contributions from the Beyond-the-Standard-Model (BSM) amplitudes, where the interplay between the strong interaction and the new BSM weak phases could not be reliably understood without the precise theoretical predictions for the QCD part.

1.1.3 Radiative Decays $\Upsilon(5S) \to \gamma W_{bJ}$

The Z_b states were discovered in single-pion transitions of $\Upsilon(5S)$ and $\Upsilon(6S)$, followed by another single-pion transition to the bottomonium states. According to molecular interpretation, $Z_b(10610)$ is primarily a $B\bar{B}^*$ state, while $Z_b(10650)$ (a.k.a. Z_b') is a $B^*\bar{B}^*$ state. Z_b are spin-1 isotriplets (both neutral and charged states were discovered in transitions $\Upsilon(nS) \to \pi Z_b$ $(n = 5, 6)$. The hypothetical partners of Z_b, *i.e.* the W_{bJ} states, would also be isotriplets but of spin zero. Therefore the W_{bJ} states are expected to appear in transitions $\Upsilon(nS) \to \rho W_{bJ}$. Conservation of angular momentum allows J in W_{bJ} to be 0, 1 or 2. Excited states such as W_{b0}' could exist as well. Quantum numbers assigned to Z_b and W_{bJ} states are summarized in Table 1.

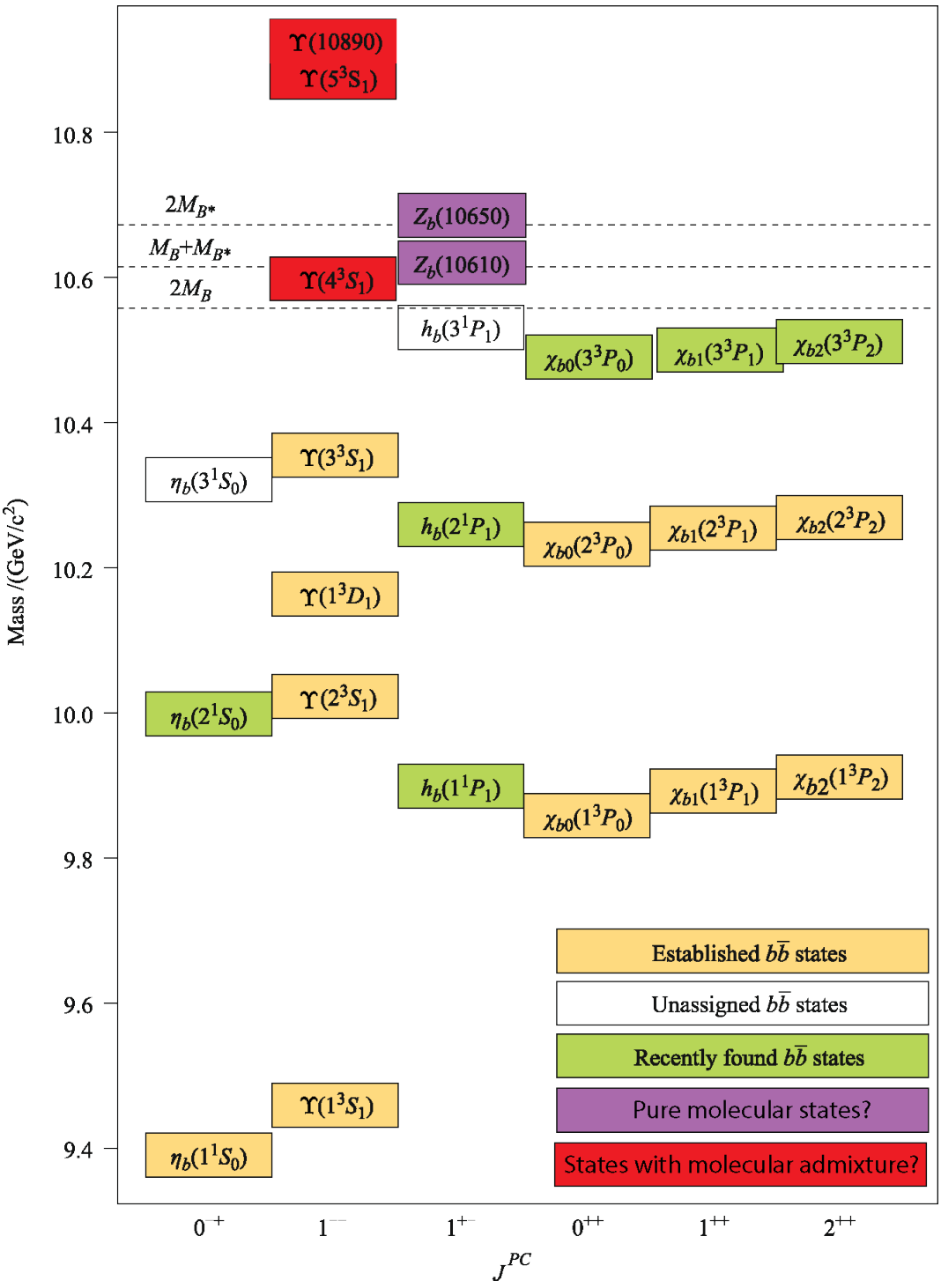

Figure 2: Most relevant (for our study) states in conventional bottomonium and bottomonium-like spectroscopies. We modified this figure from S. Olsen's review article [12].

Table 1: Molecular isotriplet states which could be produced in the decays of $\Upsilon(5S)$ and $\Upsilon(6S)$ according to [10]. Note that the ρ could be replaced by a photon in the decays of $I_3 = 0$ states, but this would suppress the expected rate even more. Please see Figure 3 as well.

$I^G(J^P)$	Name	Co-produced with (threshold, GeV/c^2)	Assumed composition	Decay channels
$1^+(1^+)$	$Z_b(10610)$	π (10.75)	$B\bar{B}^*$	$\Upsilon(nS)\pi, h_b(nP)\pi, \eta_b(nS)\rho$
$1^+(1^+)$	$Z_b'(10650)$	π (10.79)	$B^*\bar{B}^*$	$\Upsilon(nS)\pi, h_b(nP)\pi, \eta_b(nS)\rho$
$1^-(0^+)$	W_{b0}	ρ (11.34), γ (10.56)	$B\bar{B}$	$\Upsilon(nS)\rho, \eta_b(nS)\pi, \chi_b\pi$
$1^-(0^+)$	W_{b0}'	ρ (11.43), γ (10.65)	$B^*\bar{B}^*$	$\Upsilon(nS)\rho, \eta_b(nS)\pi, \chi_b\pi$
$1^-(1^+)$	W_{b1}	ρ (11.38), γ (10.61)	$B\bar{B}^*$	$\Upsilon(nS)\rho, \chi_b\pi$
$1^-(2^+)$	W_{b2}	ρ (11.43), γ (10.65)	$B^*\bar{B}^*$	$\Upsilon(nS)\rho, \chi_b\pi$

The $\Upsilon(5S)$ resonance does not have enough energy to allow the transition to W_{bJ} with sufficient amount of energy left for the two pions in the tail of the ρ invariant mass. In our analysis, instead of searching for decays with the ρ mesons, we have to allow for the $q\bar{q}$ annihilation and pay the price of approximately $\alpha_{\rm em}$ in the branching fraction:

$$\frac{\Gamma(\Upsilon(5S) \to \gamma W_{bJ})}{\Gamma(\Upsilon(5S) \to Z_b\pi)} \sim \alpha_{\rm em} \approx \frac{1}{137} \tag{1.1}$$

Therefore, we search for the transitions $\Upsilon(5S) \to \gamma W_{bJ}$. This indirect phase space limitation allows us to search only for the $I_3 = 0$ partners of the Z_b states, *i.e.* only the neutral component of each isotriplet can be found in such radiative transitions. We explain this strategy, suggested [13] by M.B. Voloshin, in Figure 3.

To search for all new resonances expected in the new spectroscopy would require to collect a sizeable data sample at $\Upsilon(6S)$ or above its energy. Such possible future studies [14] at Belle II and many more interesting discussions (such as possible existence of isoscalar partners

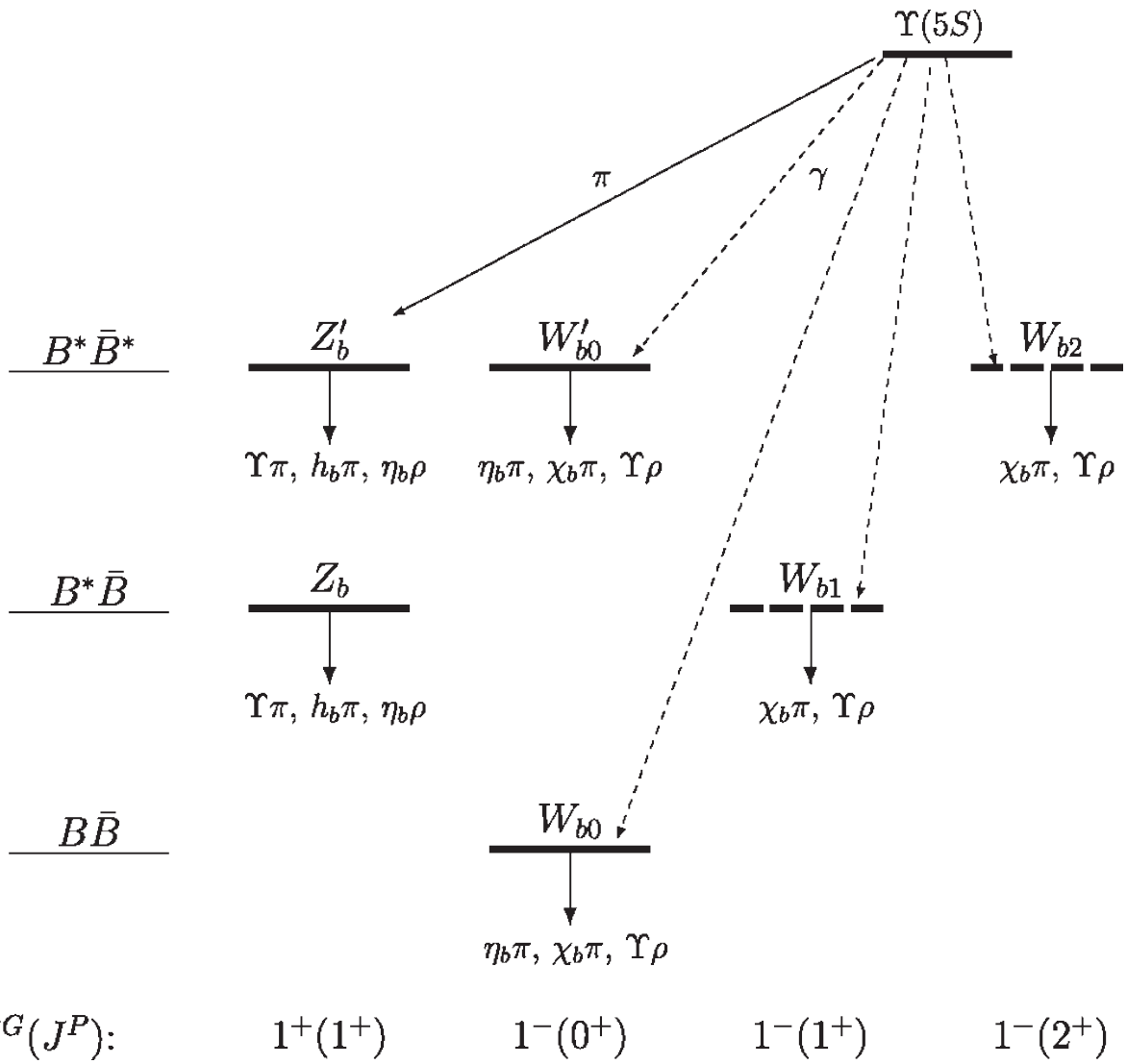

Figure 3: The expected family of isotriplet resonances from Ref. [13] (which the reader is advised to consult for relevant details). For $\Upsilon(6S)$ transitions, the photon is replaced by ρ. This would also allow to access charged W_{bJ} states. Also, please see Table 1.

of Z_b and W_{bJ}) can be found elsewhere [10]. In the rest of this paper, we focus on the analysis of the full $\Upsilon(5S)$ data sample where we design a search for the decay $\Upsilon(5S) \to \gamma W_{bJ}$.

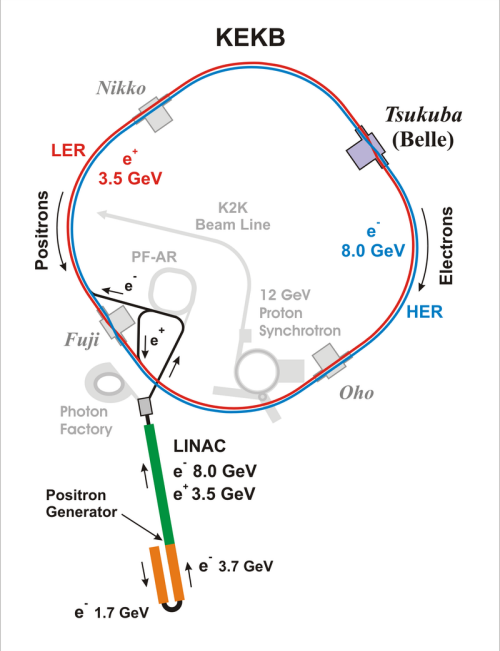

Figure 4: Schematic diagram of the KEKB collider.

1.2 The Belle Experiment

1.2.1 KEKB

The KEKB asymmetric-energy e^+e^- collider was designed to produce a large number of $B\bar{B}$ pairs at a center of mass energy of $\sqrt{s} = 10.58$ GeV and $\sqrt{s} = 10.86$ GeV, corresponding to the invariant mass of $\Upsilon(4S)$ and $\Upsilon(5S)$, respectively. A schematic diagram of the KEK accelerator complex is shown in Figure 4. Electrons and positrons are accelerated using a linear accelerator and are then injected into the high energy ring (HER) at an energy of 8.0 GeV and the low energy ring (LER) at an energy of 3.5 GeV. The HER and LER have a single intersection point (the interaction region) where the electron and positron beams are made to collide. The asymmetric energy of the electron and positron beams results in a Lorentz boost of the center of mass system, enabling time dependent measurements to be performed for B mesons produced in e^+e^- annihilation (though such measurements are not relevant to our analysis). A detailed description of the KEKB collider can be found in reference [15].

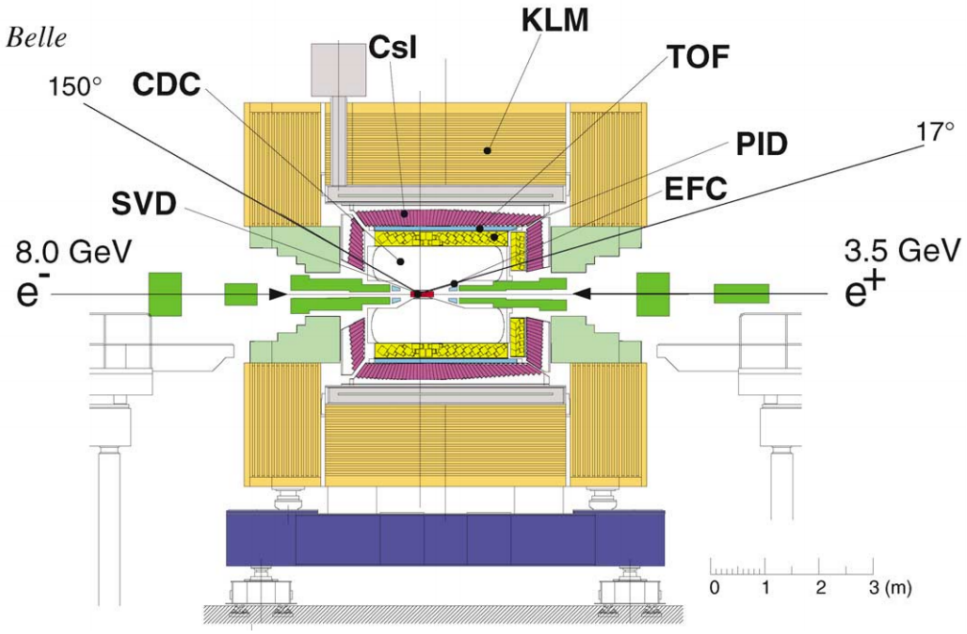

Figure 5: Schematic diagram of the Belle detector.

1.2.2 The Belle Detecctor

The Belle detector is a multilayered particle detector located at the interaction point of the KEKB collider. A schematic diagram of the Belle detector is shown in Figure 5. The detector consists of seven subdetectors. We now briefly describe each subdetector.

The silicon vertex detector (SVD) is used for vertex reconstruction and works in conjunction with the central drift chamber (CDC) to reconstruct charged tracks. The CDC is permeated by a uniform 1.5 T magnetic field directed along the beam axis. Electromagnetic showers are detected using the electromagnetic calorimeter (ECL). Charged track identification is performed using the dE/dx measurement from the CDC, the aerogel Cherenkov counters (ACC), and the time-of-flight scintillation counters (TOF). Muons and neutral kaons are detected using the K_L and muon detection system (KLM). To tune the beams, the detector is instrumented with the extreme forward calorimeter (EFC). The Belle detector and its subdetectors are described in detail in reference [16].

1.3 Analysis Techniques

1.3.1 Event Reconstruction

When $\Upsilon(5S)$ is produced in e^+e^- annhilation, it quickly decays into less massive daughter particles. Hence, it is not possible to directly detect $\Upsilon(5S)$ using the Belle detector. Instead, we detect the final state particles produced in its subsequent decays. Using energy-momentum conservation, we can calculate the the energy and momentum of the parent $\Upsilon(5S)$ by summing the energy and momenta of all of its detectable daughter particles. This process is known as event reconstruction and allows us to indirectly infer properties of the parent $\Upsilon(5S)$ without directly detecting it.

In this paper, we present a design study for $\Upsilon(5S) \to \gamma W_{bJ}$ decaying to the final state consisting of $\pi^+\pi^-\mu^+\mu^-\gamma$. To search for this process, we reconstruct candidates for the parent $\Upsilon(5S)$ using all possible combinations of the reconstructed final state particles. However, not all combinations of these final state particles come from decays of $\Upsilon(5S)$. Candidates that do not come from decays of $\Upsilon(5S)$ but have the correct final state particles are called combinatorial background. It is possible to statistically separate reconstructed candidates that do come from decays of $\Upsilon(5S)$ from combinatorial background by analyzing various distributions associated with the reconstructed candidates. For instance, the distribution of reconstructed invariant mass for actual, correctly reconstructed $\Upsilon(5S)$ candidates peaks near the mass of $\Upsilon(5S)$, while the distribution of combinatorial background does not usually exhibit such peaking behavior and could be modeled using a smooth function. By exploiting the differences between signal and background distributions for reconstructed candidates, we can statistically separate $\Upsilon(5S)$ signal from backgrounds.

1.3.2 Monte Carlo Simulation

In Monte Carlo (MC) simulation, we generate particle decay events produced in e^+e^- annihilation followed by the simulation of the Belle detector's response to the resulting final state particles. MC simulation uses pseudorandom number generators to determine which process should occur in each individual e^+e^- annihilation as well as the accuracy

of the measurements performed by the Belle dectector. The probability of a particular process to be selected by the generator is tabulated using the results of previous experimental measurements as well as theoretical predictions of the probabilities for these processes. A user can alter the probabilities for these processes, for instance, to ensure that certain processes are generated.

In our analysis, we use two types of MC samples known as signal MC and background MC. In signal MC, we generate only a certain set of decays (or possibly just one decay). In background MC, all decay processes are simulated according to their tabulated probabilities. Both signal and background MC samples are used to study differences between signal and background distributions with high statistics, allowing us to optimize our analysis techniques for use on real data.

2.0 Analysis Strategy

In this analysis, we search for a new molecular state W_{bJ} which could be produced in the transition $\Upsilon(5S) \to \gamma W_{bJ}$ followed by the decays $W_{bJ} \to \Upsilon(1S)\rho^0$, $\Upsilon(1S) \to \mu^+\mu^-$, $\rho^0 \to \pi^+\pi^-$. We select a fully-reconstructed final state particle combination $\pi^+\pi^-\mu^+\mu^-\gamma$ with an energy most consistent with the center of mass energy of the experimental run.

We now provide definitions of several quantities we use in this analysis. We use $M(X)$ to denote the invariant mass of a system X and define the invariant mass recoiling against X as

$$M_{\rm rec}(X) = \sqrt{(E_{\rm cm}(\exp) - E_{\rm cm}(X))^2 - |\vec{0} - \vec{p}_{\rm cm}(X)|^2} \tag{2.1}$$

where $E_{\rm cm}(\exp)$ is the run's average energy, and $E_{\rm cm}(X)$ and $\vec{p}_{\rm cm}(X)$ are the energy and momentum of system X. Subscript "cm" is used for quantities evaluated in the center of mass reference frame of the experiment. We define the energy difference ΔE as

$$\Delta E = E_{\rm cm}(\pi^+\pi^-(\mu^+\mu^-)_{\rm fit}\gamma) - E_{\rm cm}(\exp). \tag{2.2}$$

where subscript "fit" indicates that the muon pair is constrained the nominal mass of $\Upsilon(1S)$.

We first generate large MC samples of $\Upsilon(5S) \to \gamma W_{bJ}$ signal events. To understand the properties of background events observed by Belle, we use official $\Upsilon(5S)$ MC samples (*i.e.* generic MC). We generate several additional MC samples to investigate the effects of initial state radiation (ISR) and final state radiation (FSR) for known background processes such as, *e.g.*, $e^+e^- \to \gamma_{\rm ISR}\Upsilon(5S)$ followed by the decay $\Upsilon(5S) \to \Upsilon(1S)\pi^+\pi^-$. Using these MC samples, we identify variables that efficiently separate signal events from background events. We optimize our analysis using these MC samples before analyzing data. When applying the analysis procedure to data, we blind the region where we expect to find the signal to avoid experimenter's bias. We then observe and study discrepancies between MC simulation and blinded data sample. We use a variety of MC samples and the blinded data sample to estimate the shape of the background distribution in the blinded signal region (later defined

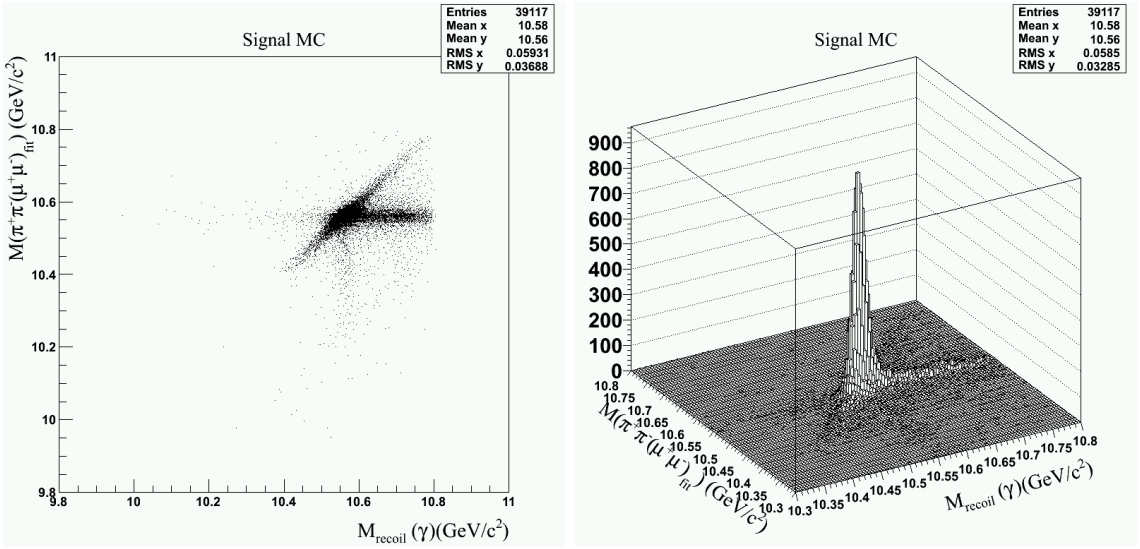

Figure 6: $M(\pi^+\pi^-(\mu^+\mu^-)_{\rm fit})$ vs $M_{\rm rec}(\gamma)$ distribution for signal MC events. Only events for process $\Upsilon(5S) \to W_{b0}\gamma$ are plotted.

in Section 5.2). To model signal and background shapes in extended unbinned maximum likelihood fitting, we use the software package RooFit [17].

To understand signal and background distributions, we investigate two invariant mass variables, $M(\pi^+\pi^-(\mu^+\mu^-)_{\rm fit})$ and $M_{\rm rec}(\gamma)$, which provide two independent ways to estimate the invariant mass of W_{bJ}. For fully reconstructed signal events (where $\Delta E \approx 0$), these two variables estimate the same quantity. Therefore, signal events fall along the main diagonal of the $M(\pi^+\pi^-(\mu^+\mu^-)_{\rm fit})$ vs $M_{\rm rec}(\gamma)$ plot shown in Figure 6. Note that ΔE is thus the most important variable we can use to select fully reconstructed signal event candidates. To extract the signal and to estimate the upper limit on the signal branching fraction, we use extended unbinned maximum likelihood method and fit the distribution of $M(\pi^+\pi^-(\mu^+\mu^-)_{\rm fit})$.

3.0 Monte Carlo and Data Samples

3.1 Signal Monte Carlo Samples

Signal MC samples for radiative decays of $\Upsilon(5S)$ to W_{b0}, W'_{b0}, and W_{b1} were generated using MC generator EvtGen [18], while the detector response is simulated using GEANT4 [19]. We did not generate a sample for W_{b2} because it is expected to have the same invaraint mass as W'_{b0}. Approximately 100,000 signal MC events were generated in each sample. W_{bJ} is generated with an intrinsic width of 15 MeV, similar to the widths of Z_b and Z'_b. Table 2 displays the decay models [20] used in Monte Carlo simulation of signal processes. The PHOTOS package [21] is used to simulated final state radiation (FSR). To allow for softer FSR photons in simulation, we modified the PHOTOS package to lower the minimum energy of final state radiation. Please see Section 9.1 for details.

Table 2: Decay models [20] used in Mote Carlo simulation of signal processes.

Decay Process	Decay Model used in Mote Carlo Simulation
$\Upsilon(5S) \to W_{bJ}\gamma$	VSP_PWAVE (decay of a vector to a scalar meson and a photon)
$W_{bJ} \to \Upsilon(1S)\rho^0$	SVV_HELAMP (decay of a scalar to two vectors)
$\rho^0 \to \pi^+\pi^-$	VSS (decay of a vector into two scalars)
$\Upsilon(1S) \to \mu^+\mu^-$	VLL (decay of a vector to a pair of charged leptons)
Final state radiation	PHOTOS (modified)

3.2 Background Monte Carlo Samples

To understand the properties of background events collected by Belle, we use Monte Carlo simulation samples of inclusive generic B decays and continuum events, referred to

as generic MC. Generic MC should provide a complete description of processes produced at Belle. There are currently six so-called "streams" of generic MC available (from experiments 43, 53, 67, 69, and 71). Each stream consists of 121.4 fb^{-1} of $\Upsilon(5S)$ resonance data and is equivalent to a full Belle data sample. We use all six streams to study background processes. Plots showing generic MC events contain events from all six streams to improve statistics for background events.

3.3 Data Sample

In this analysis, we use the full 121.4 fb^{-1} of on-resonance $\Upsilon(5S)$ data. This dataset corresponds to $(6.53 \pm 0.66) \times 10^6$ $B_s\bar{B}_s$ pairs collected by the Belle detector at the KEKB collider from asymmetric energy e^+e^- collisions with $\sqrt{s}$ = 10.86 GeV [22]. We blind the region where we expect the signal to peak in the 2-dimensional distribution of $M(\pi^+\pi^-(\mu^+\mu^-)_{\rm fit})$ vs $M_{\rm rec}(\gamma)$. This blinded region is defined and discussed in Section 5.2.

4.0 Selection Criteria

4.1 Selection of Photon Candidates

Photons are detected and reconstructed using the electromagnetic calorimeter (ECL). A schematic diagram of the ECL is shown in Figure 7. The ECL consists of a barrel section and two forward and backward endcap sections lined with scintillating cesium iodide crystals doped with thalium (CsI(Tl)) oriented towards the beam interaction point. The ECL covers polar angles within the range $17^\circ < \theta < 150^\circ$. There exist small gaps between the barrel and forward and backward calorimeters to provide room for support structures, therefore reducing solid angle coverage.

At high energies, photons interact with the CsI(Tl) crystals and undergo pair production. The resulting electron and positron emit additional photons via bremmsstrahlung which in turn interact with the crystals and undergo pair production. This repeated process of pair production followed by bremsstrahlung produces what is known as an electromagnetic "shower." Energy deposits from these showers are used to reconstruct photons. The CsI(Tl) crystals have a length of 30 cm, or equivalently 16.2 radiation lengths, where the radiation length is defined as the mean distance over which an electron's energy decreases due to bremmsstrahlung by a factor of e. The mean distance a photon will travel before pair producing, *i.e.* the conversion length, is proportional to the radiation length. The crystals provide an excellent photon energy resolution $\sigma_E/E = 2.5\%$ where E is measure in units of GeV.

To select reconstructed photon candidates, we use the E_9/E_{25} ratio. The E_9/E_{25} ratio is defined as the energy summed in the 3 x 3 array of crystals surrounding the center of the shower (E_9) to that of the 5 x 5 arrays of crystals surrounding the center of the shower (E_{25}). We require that photons candidates have $E_9/E_{25} > 0.75$ and $17^\circ < \theta < 150^\circ$. We additionally require reconstructed photons to have energy between 100 and 600 MeV. We require that signal event candidates contain at least one such photon.

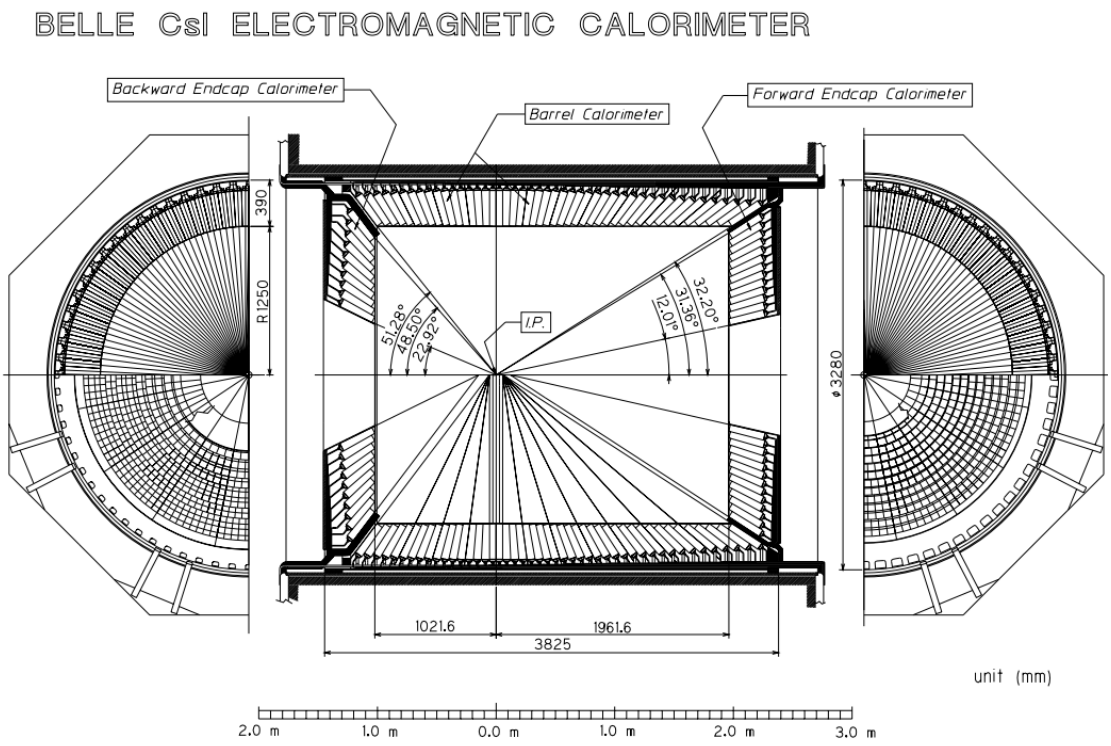

Figure 7: Schematic diagram of the ECL.

4.2 Selection of Pion and Muon Candidates

The central drift chamber (CDC) is used to reconstruct charged particle tracks and determines their momenta. Furthermore, the CDC measures the specific energy loss of charged particles by ionization per unit distance, dE/dx, which is used in particle identification.

The CDC is filled with a gas mixture of 50% helium and 50% ethane and contains "field" and "sense" wires thoughout its volume. Negatively biased field wires are positioned around positively biased sense wires and create an electric field surrounding the sense wires. When a charged particle passes through the CDC, it ionizes the gas, and the resulting ionization electrons drift towards the sense wires while the positive ions drift towards the field wires. The electric field accelerates the ionized electrons and provides them with the energy to ionize additional gas atoms. This avalanche effect amplifies the electric signal detected by the sense wires and prompts a detector response called a "hit." A charged particle produces multiple hits as it passes through the CDC which are used to reconstruct its trajectory.

Table 3: Efficiency for various particle identification likelihood ratios.

Likelihood Ratio	Efficiencies (for momentum greater than 1 GeV/c)
$R_{K,\pi}$	>80%
$R_{e,hadron}$	>90%
R_{μ}	>90%

Because a magnetic field is present in the CDC, charged tracks follow a helical trajectory. A charged particle's momentum is reconstructed from the curvature of its trajectory. The CDC provides a momentum resolution of $\sigma_{p_t}/p_t = 0.3\%\sqrt{p_t^2 + 1}$, where p_t is in GeV/c.

The electric signal from the hit is also used to determine number of electrons originally ionized by the charged particle and thus the energy loss per unit distance dE/dx of the charged particle. The Bethe-Bloch formula [23] describes the mean energy loss $\langle$dE/dx$\rangle$ per unit distance and depends on the momentum of the charged particle. Hence, measuring dE/dx allows to distinguish between different charged particles. The CDC provides a dE/dx resolution of $\frac{\sigma_{\mathrm{dE/dx}}}{\mathrm{dE/dx}} = 6\%$.

Hadrons such as pions strongly interact with detector material, producing showers. Hence, pions lose most of their energy through interactions with the detector material and never reach the outermost components of the detector. One the other hand, muons with sufficiently large momentum do not strongly interact with the detector material in the CDC (as muons are leptons) and pass through all inner detector components. The K_L and muon detection system (KLM) is used to identify muons (as well as long-lived neutral kaons). Hits in the CDC that correspond to hits in the KLM are likely to be due to muons.

We require that reconstructed trajectories (*i.e.* tracks) of pion and muon candidates satisfy $dr < 0.3$ cm and $|dz| < 2$ cm, where dr and dz are defined as the distances from the interaction point to the point of track's closest approach in the radial and beam axis directions, respectively. We also require pion and muon candidates to have transverse momenta $p_T > 100$ MeV. Pion candidates must satisfy $R_{K,\pi} < 0.9$, where $R_{K,\pi}$ is the "Kaon identification variable" defined as the likelihood ratio of the charged track to be due to a kaon versus

a pion, and $R_{e,hadron} < 0.9$, where $R_{e,hadron}$ is the likelihood ratio of the charged track to be due to an electron versus a hadron. Similarly, muon candidates must satisfy $R_\mu > 0.1$, where R_μ is the likelihood ratio of the charged track to be due to a muon versus other particles detected by the KLM detector subsystem. Efficiencies for each of these identification variables can be found in Table 3. After imposing the aforementioned requirements, we additionally require there to be four unique charged tracks – two pions and two muons. Events with more than four such tracks are rejected.

4.3 Selection of ρ^0 Candidates

We reconstruct ρ^0 meson candidates using the decay channel $\rho^0 \to \pi^+\pi^-$. This decay has a branching fraction $\mathcal{B}(\rho^0 \to \pi^+\pi^-) = 0.998$. We require ρ candidates to have an invariant mass between 0.420 GeV/c^2 and 1.020 GeV/c^2.

4.4 Selection of $\Upsilon(1S)$ Candidates

We reconstruct $\Upsilon(1S)$ candidates using the decay channel $\mu^+\mu^-$. This decay has a branching fraction $\mathcal{B}(\Upsilon(1S) \to \mu^+\mu^-) = 0.0248$. We require $\Upsilon(1S)$ candidates to have an invariant mass between 9.3 GeV/c^2 and 9.6 GeV/c^2. The invariant mass of such muon pairs is then constrained to $\Upsilon(1S)$ nominal mass of 9.460 GeV/c^2 using the class *kmassfitter* of the *KFitter* package.

4.5 Selection of $\Upsilon(5S)$ Candidates

We reconstruct $\Upsilon(5S)$ candidates using the decay channel $\Upsilon(5S) \to \gamma W_{bJ}$. $\Upsilon(5S)$ has a nominal invariant mass of 10.860 GeV/c^2. We require $\Upsilon(5S)$ candidates to have an invariant mass between 10.2 GeV/c^2 and 11.5 GeV/c^2. We require signal event candidates to contain

Table 4: Selection criteria for $\Upsilon(5S) \to \gamma W_{bJ}$

Particle Candidate	Selection Criteria
γ	100 MeV $E(\gamma) < 600$ MeV
$\pi^{\pm}, \mu^{\pm}$	$dr < 0.3$ cm $\lvert dz \rvert < 2$ cm $p_T > 100$ MeV/c
$\pi^{\pm}$ PID	$R_{K,\pi} < 0.9$ $R_{e,hadron} < 0.9$
$\mu^{\pm}$	$R_{\mu} > 0.10$
ρ^0	0.420 GeV/c^2 $< M(\pi^+\pi^-) <$ 1.020 GeV/c^2
$\Upsilon(1S)$	9.3 GeV/c^2 $< M(\mu^+\mu^-) <$ 9.6 GeV/c^2
$\Upsilon(5S)$ (full event reconstruction)	10.2 GeV/c^2 $< M(\rho^0\gamma) <$ 11.5 GeV/c^2 -0.05 GeV $< \Delta E < 0.03$ GeV Exactly four tracks: two muons and two pions

exactly two pion and two muon candidates. A summary of our selection criteria is shown in Table 4.

4.6 Best Candidate Selection

Approximately 32% of signal MC events satisfying our selection criteria have multiple signal candidates. This is exclusively due to relatively soft photons. In events with multiple signal candidates, we select the candidate that has ΔE closest to zero. The selected candidates are correctly MC-tagged to full MC truth for signal 90% of the time. For fully re-

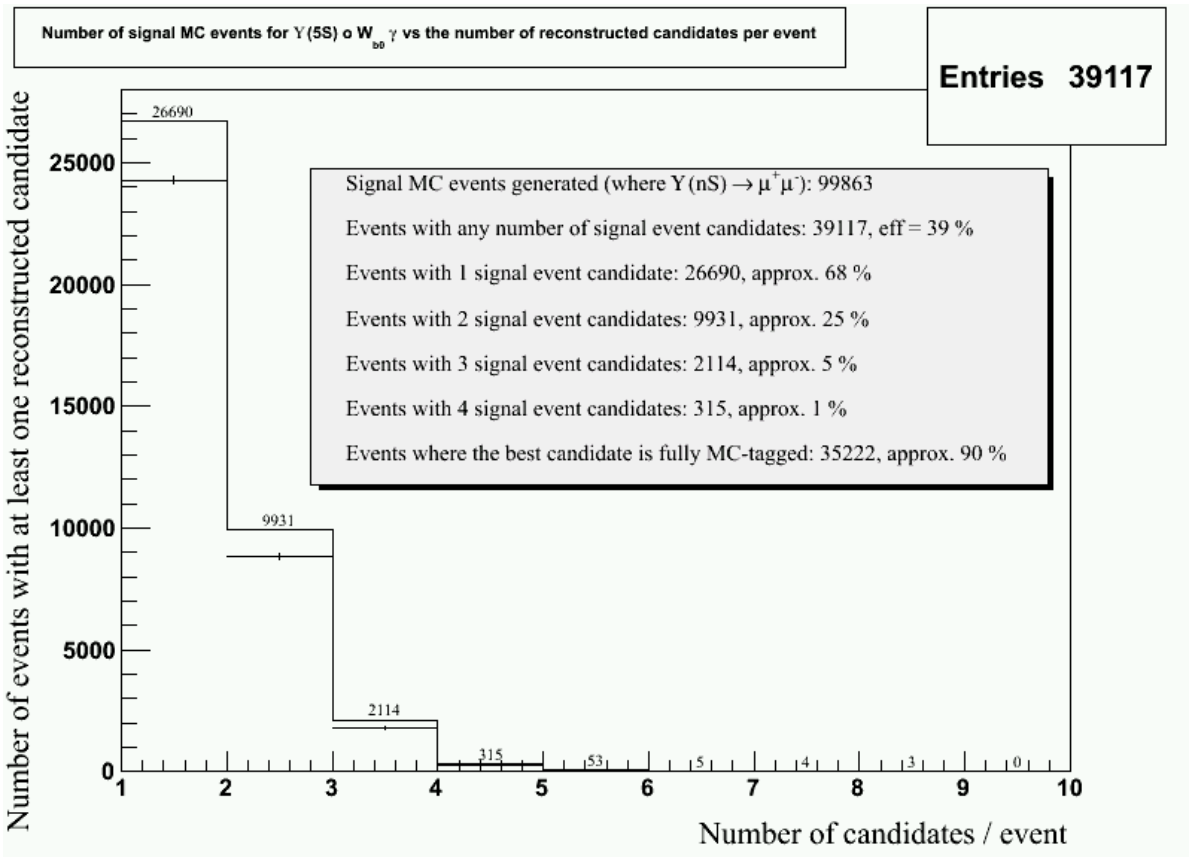

Figure 8: Number of candidates per event and the probabilities to correctly MC-tag the best candidate.

constructed signal MC events with multiple candidates, our best candidate selection method selects a candidate correctly MC-tagged to full MC truth 88% of the time. Statistics quantifying the frequency of multiple candidates and the probability to identify the correct particle combinations through MC tagging are shown in Figure 8. All figures in this document show distributions of the best event candidate satisfying all selection criteria.

5.0 Signal Monte Carlo Studies

5.1 Signal Monte Carlo Distributions

The variables that provide the best separation between signal and backgrounds are $M_{\rm recoil}(\gamma)$ and $M(\pi^+\pi^-(\mu^+\mu^-)_{\rm fit})$. For signal events these variables provide two independent ways to estimate the invariant mass of W_{bJ}. Hence, fully reconstructed signal events fall along the main diagonal of the $M(\pi^+\pi^-(\mu^+\mu^-)_{\rm fit})$ vs $M_{\rm rec}(\gamma)$ plot. There are two effects contributing to the observed width of $M(\pi^+\pi^-(\mu^+\mu^-)_{\rm fit})$: (1) the intrinsic width of W_{bJ}, and (2) the charged track reconstruction. Contribution to resolution from charged track reconstruction is primarily due to pions, since muon pairs are fitted to $\Upsilon(1S)$ invariant mass. The distribution of $M_{\rm rec}(\gamma)$ has a long tail due to an underestimation of photon energy, causing an overestimation of $M_{\rm rec}(\gamma)$. Effects contributing to the observed width of $M_{\rm rec}(\gamma)$ include (1) intrinsic width of W_{bJ}, and (2) photon energy resolution. $M_{\rm rec}(\gamma)$ resolution is dominated by photon energy resolution. Effects contributing to the observed shape of ΔE include (1) photon energy resolution, (2) charged track resolution, (3) beam energy resolution, and (4) the intrinsic width of W_{bJ}. ΔE resolution is dominated by photon energy resolution. The values of relevant widths are listed in Table 5.

In signal MC we observe $\sigma_{\Delta E} \approx 12$ MeV, so we take advantage of this excellent energy

Table 5: Quantities contributing to widths of observed quantities

Quantity	Value
Intrinsic width of W_{bJ}	15 MeV/c^2
Charged track resolution	4 MeV
Photon energy resolution	8 MeV
Beam energy resolution	6 MeV

resolution to select fully reconstructed events. Because the distribution of ΔE is asymmetric (primarily due to leakage from the calorimeter and relatively soft non-signal photons in signal events), we use an asymmetric selection and require $-0.05\,(\mathrm{GeV}) \leq \Delta E \leq 0.03\,\mathrm{GeV}$. This selection cuts out the long tail in the distriubtion of $M_{\mathrm{rec}}(\gamma)$ and reduces the efficiency by 20%. Note, however, that this selection primarily removes events where signal photon candidate is not reconstructed. After applying this selection on ΔE, signal reconstruction efficiency becomes approximately 31%. Distributions of line shapes and resolutions are shown in Figure 9.

5.2 Description of the Signal Region

We define three important regions: the blinded region, the signal region, and the grand sideband region. First, we define the region where we expect to find signal. We blind this region in data and refer to it as the blinded region. We define the blinded region in terms of variables $M(\pi^+\pi^-(\mu^+\mu^-)_{\mathrm{fit}})$ and $M_{\mathrm{rec}}(\gamma)$. The invariant mass of W_{b0}, W_{b1}, and W'_{b0} and W_{b2} are expected to be at the $B\overline{B}, B^*\overline{B}$, and $B^*\overline{B^*}$ thresholds respectively. The signal region is defined by the region between the $B\overline{B}$ and $B^*\overline{B^*}$ thresholds plus an additional margin of 7 MeV on either side. This corresponds to $10.49\,\mathrm{GeV/c^2} \leq M(\pi^+\pi^-(\mu^+\mu^-)_{\mathrm{fit}}) \leq 10.72\,\mathrm{GeV/c^2}$. The boundary on the left side of the region is defined by the sloped line $M_{\mathrm{rec}}(\gamma) \geq M(\pi^+\pi^-(\mu^+\mu^-)_{\mathrm{fit}}) - 0.04$ GeV/c^2 which lies parallel to the main diagonal. Approximately 20% of signal events are located in the long right tail of the distribution of $M_{\mathrm{rec}}(\gamma)$. A phase space boundary on the right side of the plot at $M_{\mathrm{rec}}(\gamma) \approx 10.8$ GeV/c^2 forces this long tail of the $M_{\mathrm{rec}}(\gamma)$ distrubtion into a smaller region for the higher mass W_{bJ} states. Hence, we do not define a sloped boundary line as the right side of the signal region – a diagonal boundary would exclude more signal events for the lower mass states because of the aforementioned phase space boundary compressing the tail. Instead, we define the vertical line boundary $M_{\mathrm{rec}}(\gamma) \leq 10.72$ GeV/c^2 which assures that approximately equal percentages of signal events would be blinded for all masses of W_{bJ} states.

We define the signal region as the region contained within $10.49\,\mathrm{GeV/c^2} \leq M(\pi^+\pi^-(\mu^+\mu^-)_{\mathrm{fit}}) \leq$

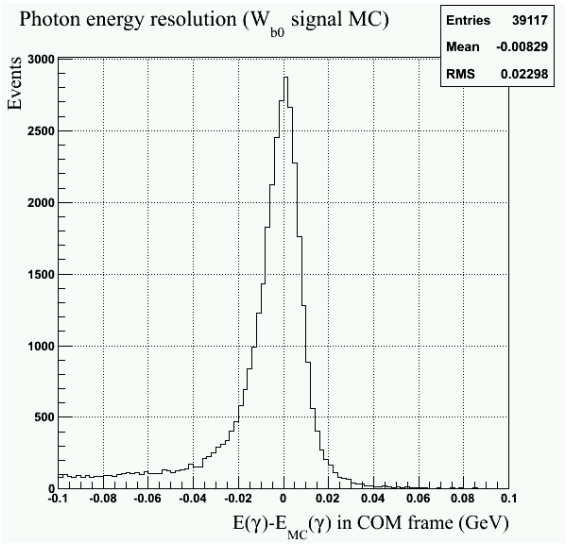

(a) Signal photon energy line shape in the center of mass reference frame.

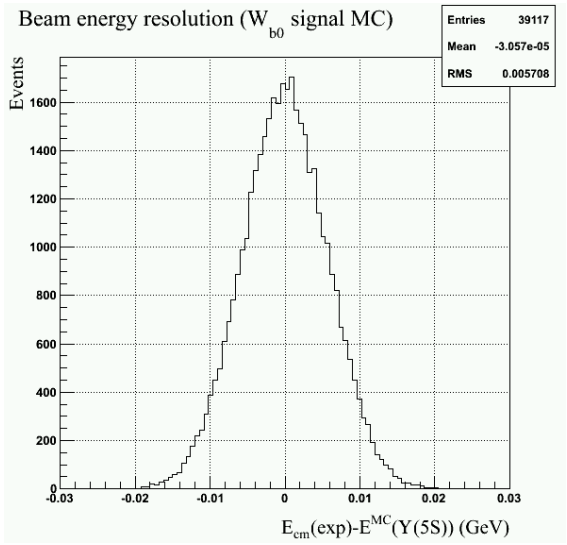

(b) Beam energy resolution.

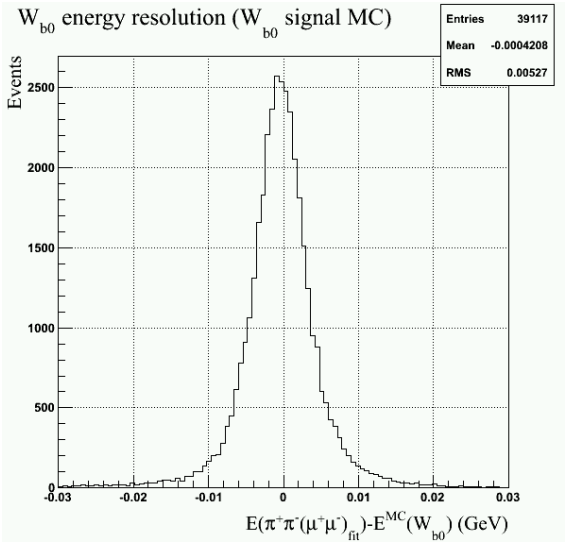

(c) $M(\pi^+\pi^-(\mu^+\mu^-)_{\rm fit})$ energy line shape (includes the effect of intrinsic W_{bJ} width and charged track reconstruction).

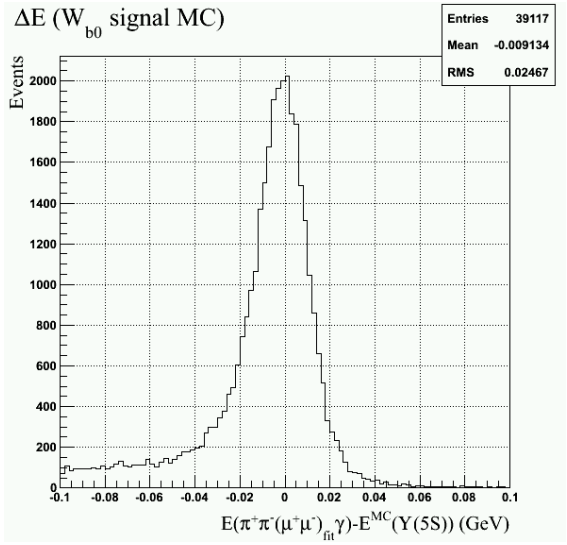

(d) Signal candidate energy line shape. Includes the effects of W_{bJ} intrinsic width and resolution.

Figure 9: Resolutions for W_{b0} signal MC.

$10.72\,\mathrm{GeV/c^2}$ satisfying $-0.05\,(\mathrm{GeV}) \leq \Delta E \leq 0.03\,\mathrm{GeV}$. The signal region is a subset of the blinded region. The ΔE requirement is effectively equivalent to reducing the blinded region to a smaller parallelogram. We additionally define the grand sideband region as the region within $10.38\,\mathrm{GeV/c^2} \leq M(\pi^+\pi^-(\mu^+\mu^-)_{\rm fit}) \leq 10.80\,\mathrm{GeV/c^2}$ satisfying

$-0.20\,\mathrm{GeV} \leq \Delta E \leq 0.20\,\mathrm{GeV}$. This region is used when studying data. Figure 10 displays these three regions with our three different signal MC samples.

It is important to note that the blinded region is not completely contained within the grand sideband region and the signal region is not completely contained within the blinded region. This due to historical reasons, as the blinded region was defined prior to the use of ΔE in this analysis.

5.3 Trigger Simulation

Relatively low final state particle multiplicity of our signal events requires us to investigate the trigger efficiency. Trigger efficiency is simulated after full reconstruction. We find correlations between trigger efficiency and kinematics. For all generated signal MC events, trigger efficiency is approximately 96%. However, when one of the muons is at a small angle with respect to the beam axis ($|\cos(\theta)| \geq 0.8$), trigger efficiency drops to approximately 89%. After accounting for trigger efficiency, our overall reconstruction efficiency drops from 31% to 29%.

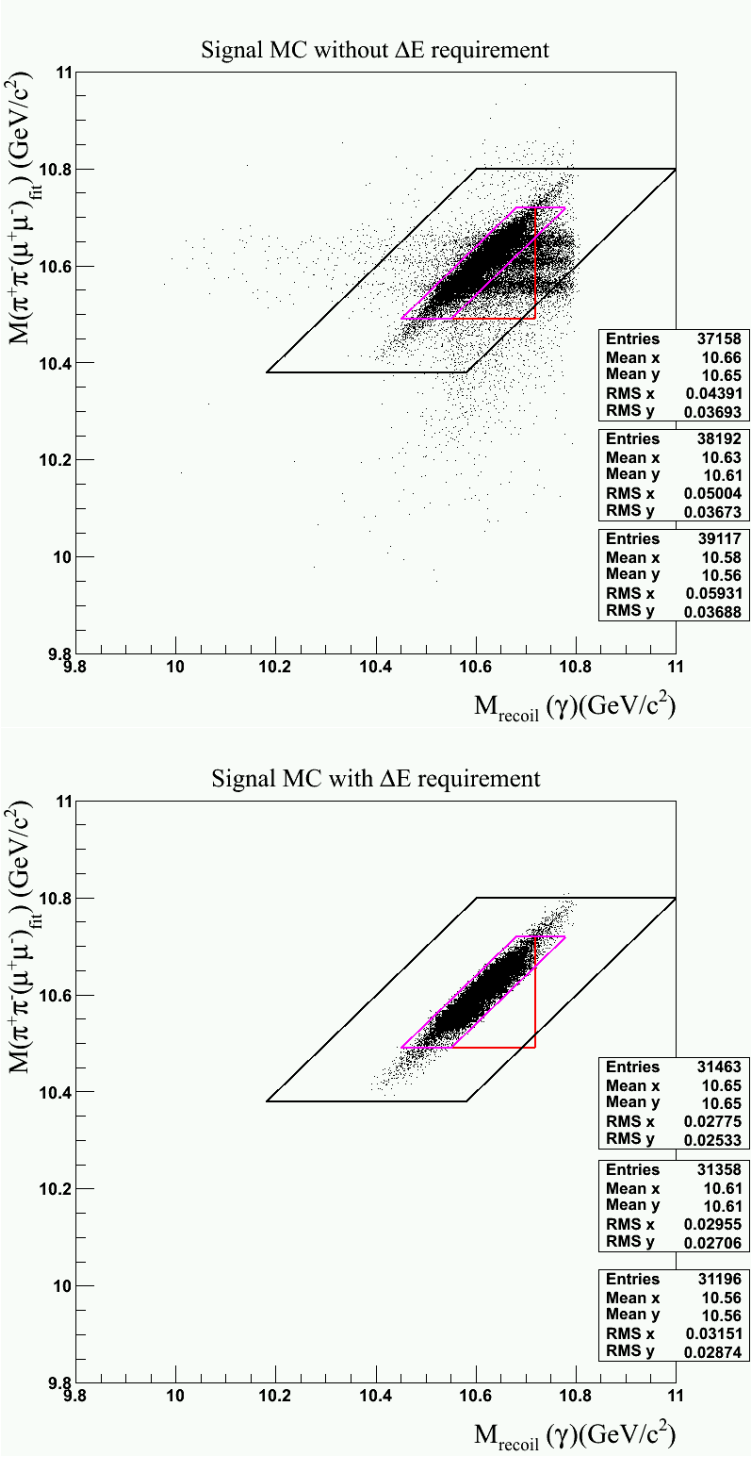

Figure 10: The blinded region (red), signal region (magenta), and the grand sideband region (black). The plot on the right includes the aforementioned ΔE requirement, while the plot on the left does not. From top to bottom, the statistics boxes correspond to W'_{b0}, W_{b1}, and W_{b0} signal MC, respectively.

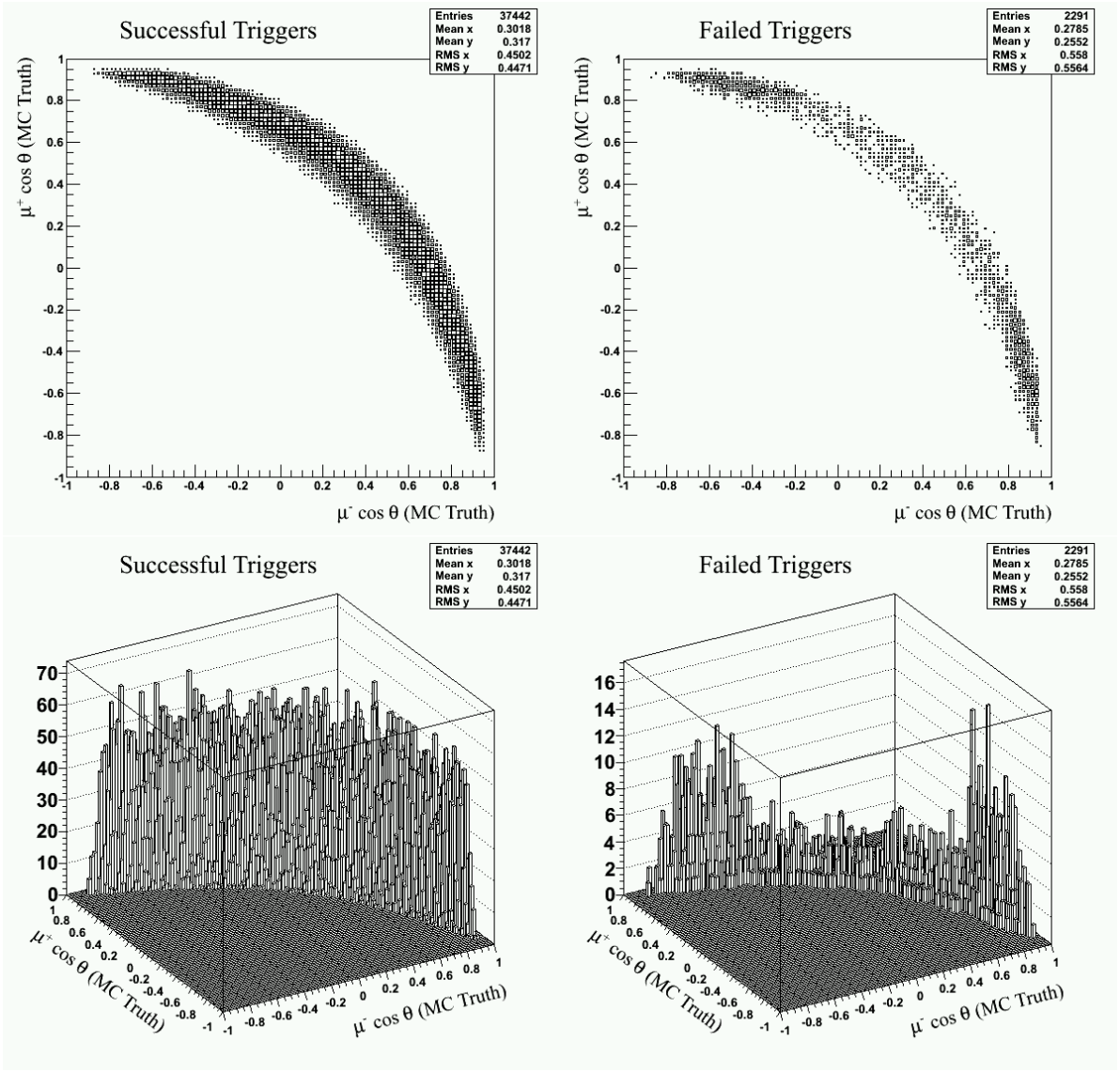

Figure 11: Reconstructed signal MC events that satisfy the offline trigger selection are plotted on the left, while events that fail the offline trigger selection are plotted on the right. We observe that events satisfying the trigger criteria are distributed more or less uniformly for kinematically allowed muons, but events failing to satisfy the trigger criteria are more likely to have one of the muons along the beam axis.

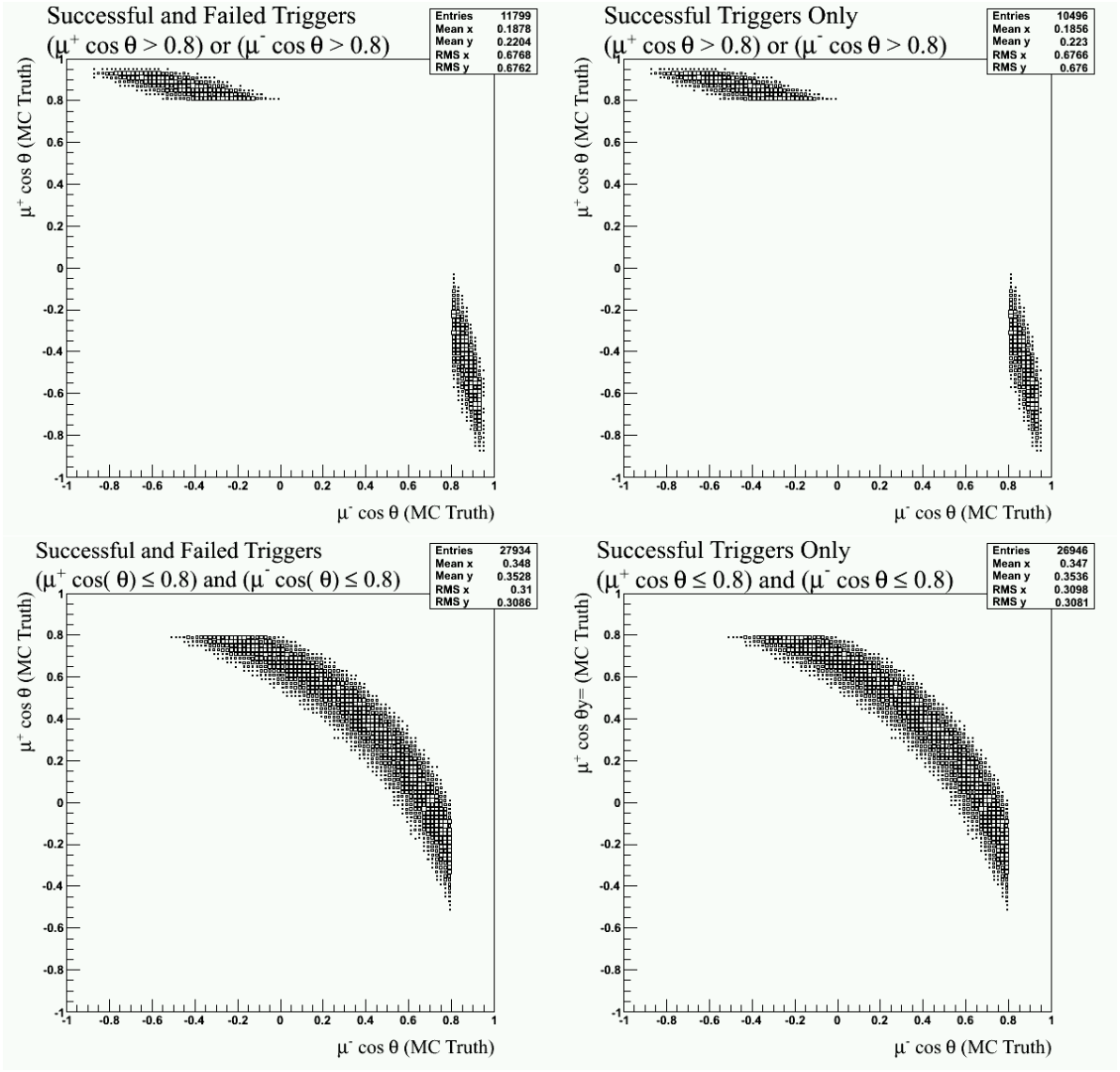

Figure 12: All reconstructed events in which neither muon is generated along the beam axis are plotted in the bottom two figures. Trigger efficiency for such events is approximately $(96 \pm 4)\%$. In the top two figures, we plot all reconstructed events where one of the muons is generated along the beam axis. Trigger efficiency for these events is reduced to about $(89 \pm 4)\%$.

6.0 Background Studies

6.1 Generic Monte Carlo and Blinded Data Studies

No *uds*, charm, or B_sB_s generic MC events pass our selection criteria. A large number of non-B_sB_s events do satisfy our selection criteria, though they fall primarily outside the signal region. The ΔE requirement excludes most of these background events. Using MC truth, we identify the background decays and group them into eight categories which are defined in Table 6. We show these background events and label them according to these categories in Figure 13. The most prominent non-B_sB_s background sources are (cascade)

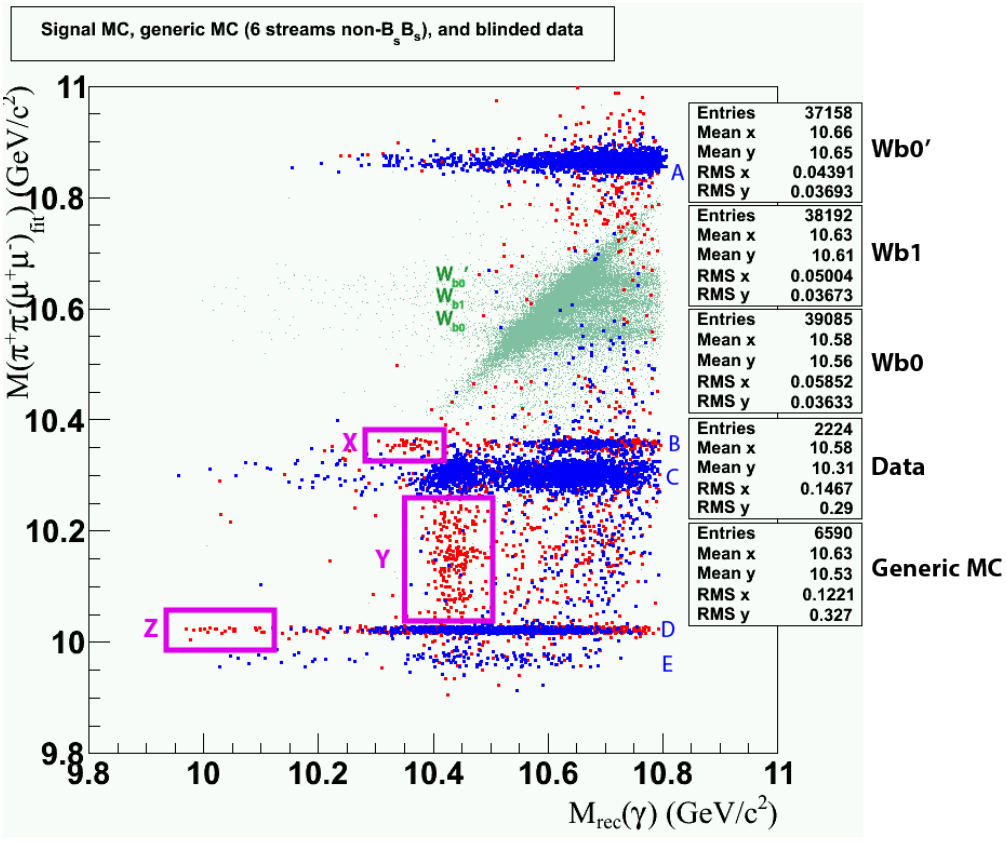

Figure 13: W_{b0}, W_{b1}, and W'_{b0} signal MC (light green), six streams of non-B_sB_s generic MC (blue), and data with the signal region blinded (red).

Table 6: Backgrounds labeled in Figure 13

Label	Background
A	$\Upsilon(5S) \to \Upsilon(1S)\pi^+\pi^- \to \mu^+\mu^-\pi^+\pi^-$
B	$\Upsilon(5S) \to \Upsilon(3S)\pi^+\pi^- \to \Upsilon(1S)\pi^+\pi^-\pi^+\pi^- \to \mu^+\mu^-\pi^+\pi^-\pi^+\pi^-$ $\Upsilon(5S) \to \Upsilon(3S)\pi^0\pi^0 \to \Upsilon(1S)\pi^+\pi^-\pi^0\pi^0 \to \mu^+\mu^-\pi^+\pi^-\pi^0\pi^0$
C	$\Upsilon(5S) \to \Upsilon(2S)\pi^+\pi^- \to \Upsilon(1S)\pi^+\pi^-\pi^+\pi^- \to \mu^+\mu^-\pi^+\pi^-\pi^+\pi^-$ $\Upsilon(5S) \to \Upsilon(2S)\pi^+\pi^- \to \Upsilon(1S)\pi^0\pi^0\pi^+\pi^- \to \mu^+\mu^-\pi^0\pi^0\pi^+\pi^-$
D	$\Upsilon(5S) \to \Upsilon(2S)\pi^0\pi^0 \to \Upsilon(1S)\pi^+\pi^-\pi^0\pi^0 \to \mu^+\mu^-\pi^+\pi^-\pi^0\pi^0$
E	$\Upsilon(5S) \to \Upsilon(3S)\pi^+\pi^- \to \Upsilon(1S)\pi^0\pi^0\pi^+\pi^- \to \mu^+\mu^-\pi^0\pi^0\pi^+\pi^-$
X	$e^+e^- \to \Upsilon(3S)\gamma \to \Upsilon(1S)\pi^+\pi^-\gamma \to \mu^+\mu^-\pi^+\pi^-\gamma$
Y	Various processes involving $\chi_{bJ}(1P) \to \gamma\Upsilon(1S)$, *e.g.* $\Upsilon(5S) \to \Upsilon(1D)\pi^+\pi^-$, where $\Upsilon(1D) \to \gamma\chi_{bJ}(1P)$
Z	$e^+e^- \to \Upsilon(2S)\gamma \to \Upsilon(1S)\pi^+\pi^-\gamma \to \mu^+\mu^-\pi^+\pi^-\gamma$

dipion transitions to $\Upsilon(1S)$. We observe an enhancement in generic MC within the blinded region due to the decay $\Upsilon(5S) \to \Upsilon(2S)\pi^+\pi^-, \Upsilon(2S) \to \Upsilon(1S)\pi^+\pi^-$ where the selected signal pion candidates did not come from the same parent. The enhancement is removed when the ΔE constraint is applied, as such background events are not fully reconstructed.

Data events outside of the blinded region are plotted in Figure 13 and listed in Table 6 as well. We compare event distributions and shapes in various regions of phase space between data and generic MC. We observe several regions where data events are clustering while generic MC events are not. While investigating these regions, we have identified the likely origins of these background events. The regions labeled 'X' and 'Z' in Figure 13 are populated by events which are due to radiative returns to a lower mass $\Upsilon(nS)$ where the radiative photon is selected as our signal photon candidate. These events are fully reconstructed,

and thus fall along the main diagonal of the plot. The region labeled 'Y' includes processes involving radiative decays of $\chi_{bJ}(1P)$. These events have additional final state particles that we do not include in signal final state reconstruction, and hence these events fall below the main diagonal where $\Delta E < 0$.

6.2 Initial State Radiation (ISR)

6.2.1 Motivation for ISR Studies

We observe that the numbers of data events do not scale uniformly with generic MC in different parts of phase space within the grand sideband region (and outside the blinded region). In particular, we find that dipion transitions to $\Upsilon(1S)$ (labeled 'A' in Figure 13) have a much longer tail in data than in generic MC. This difference is shown in Figure 14, and this is due to initial state radiation (ISR). This tail contaminates the signal region, so we generate additional MC samples with ISR to study these backgrounds. While ISR studies improve the quality of our analysis and provide us with useful information about the shape of this background in the signal region, including ISR into our analysis did not sufficiently improve the scaling between data and MC in different regions of grand sideband. Hence, the inclusion of ISR studies does not allow us to use MC simulation to make reliable predictions about the number of background events expected in the signal region in data.

6.2.2 Reweighting ISR Monte Carlo

The VectorISR model [20] is used to simulate ISR. There are two contributions to ISR photon energy when using the VectorISR model:

1. The radiator function
2. The line shape for e^+e^- annihilation to $\Upsilon(5S)$

The radiator function implemented in MC simulation does not depend on ISR photon energy, so we reweight the spectrum according to the correct radiator function up to order

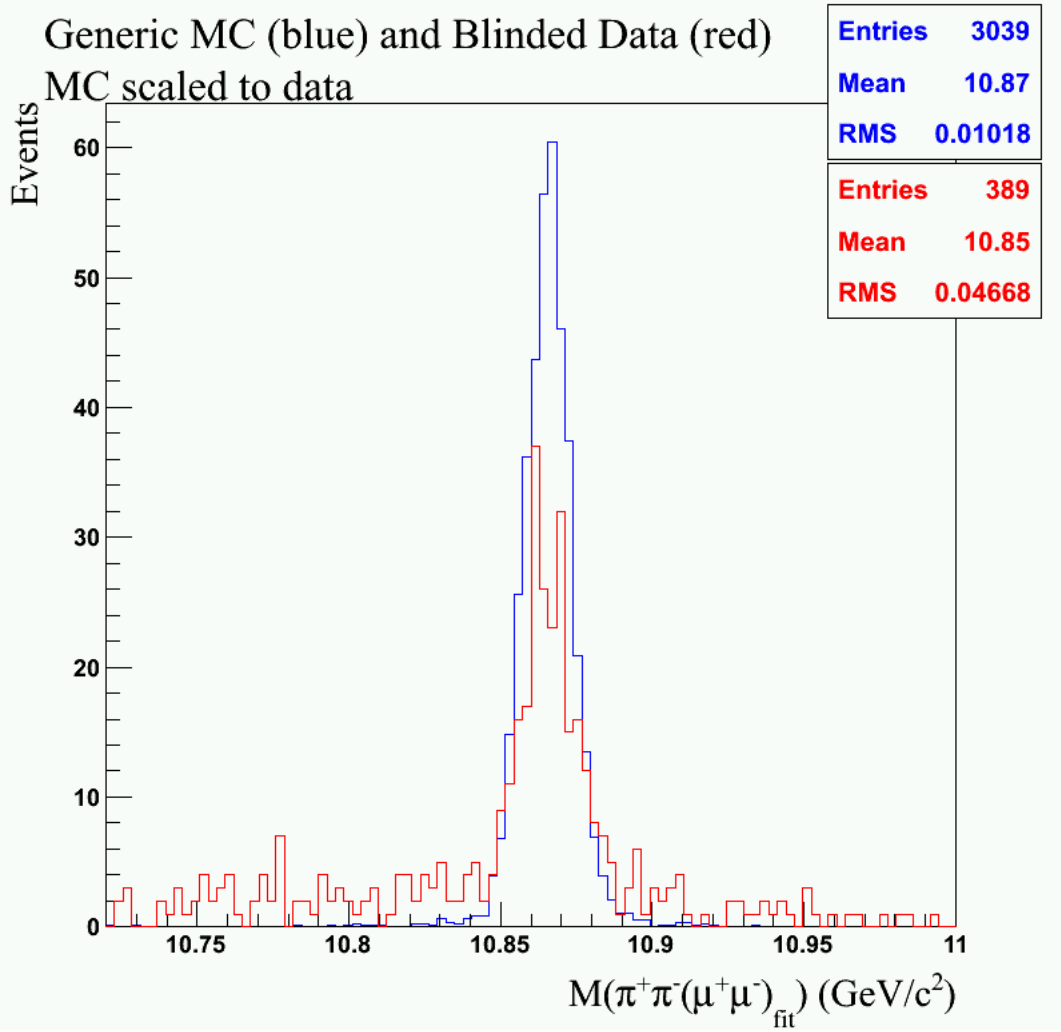

Figure 14: $M(\pi^+\pi^-(\mu^+\mu^-)_{\rm fit})$ distributions for $\Upsilon(5S) \to \Upsilon(1S)\pi^+\pi^-$ events (label 'A' in Table 6). Distributions for generic MC and blinded data are shown in blue and red, respectively. Generic MC does not include ISR and is normalized to the number of data events shown in the plotted range. We choose 10.72 GeV/c^2 as the lower limit of the range plotted, since lower masses would include the blinded region.

α^2 [24]. To implement reweighting, we divide the ISR photon energy fraction range between 0 to 0.2 in 1200 bins. We do not consider energy fractions beyond 0.2 because the ISR spectrum is truncated at 0.2. This truncation happens because the $\Upsilon(5S)$ line shape is truncated in MC at very low masses. We choose 1200 bins to assure that each bin is at most 1 MeV wide. We then analytically calculate the area under the radiator function within each

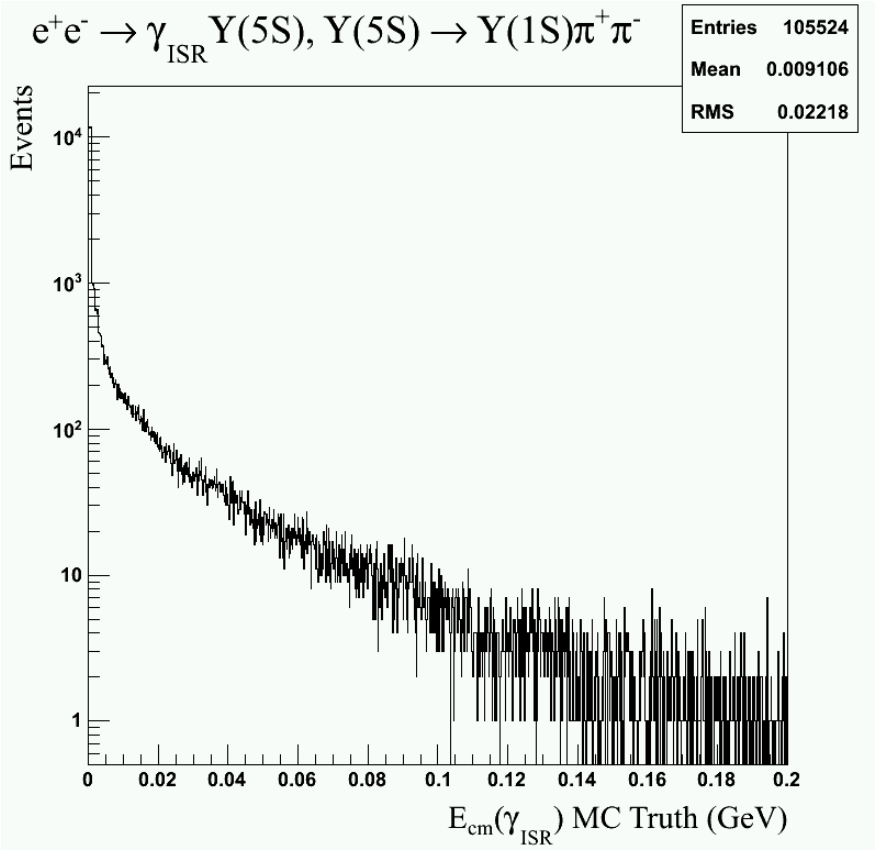

Figure 15: Reweighted ISR energy spectrum for $e^+e^- \to \gamma_{\rm ISR}\Upsilon(5S), \Upsilon(5S) \to \Upsilon(1S)\pi^+\pi^-$. Note that a log scale is used for the vertical axis.

individual bin and normalize these values to the area of the first bin. When an MC event is generated, the following accept/reject procedure is carried out:

1. We determine which bin the generated photon energy fraction falls into.
2. A random number between 0 and 1 is generated according to a uniform distribution.
3. If this number is less than or equal to the normalized area associated with the bin (which was previosly calculated and stored), the event is accepted. Otherwise, the event is rejected.

Efficiency of the accept/reject procedure is approximately 2%. To assure that we have a sizeable amount of events in our ISR MC, we generate 5,000,000 events for $\Upsilon(5S) \to \Upsilon(1S)\pi^+\pi^-$ with ISR. After running the procedure, roughly 100,000 events remain. A distribution of the reweighted ISR spectrum is shown in Figure 15.

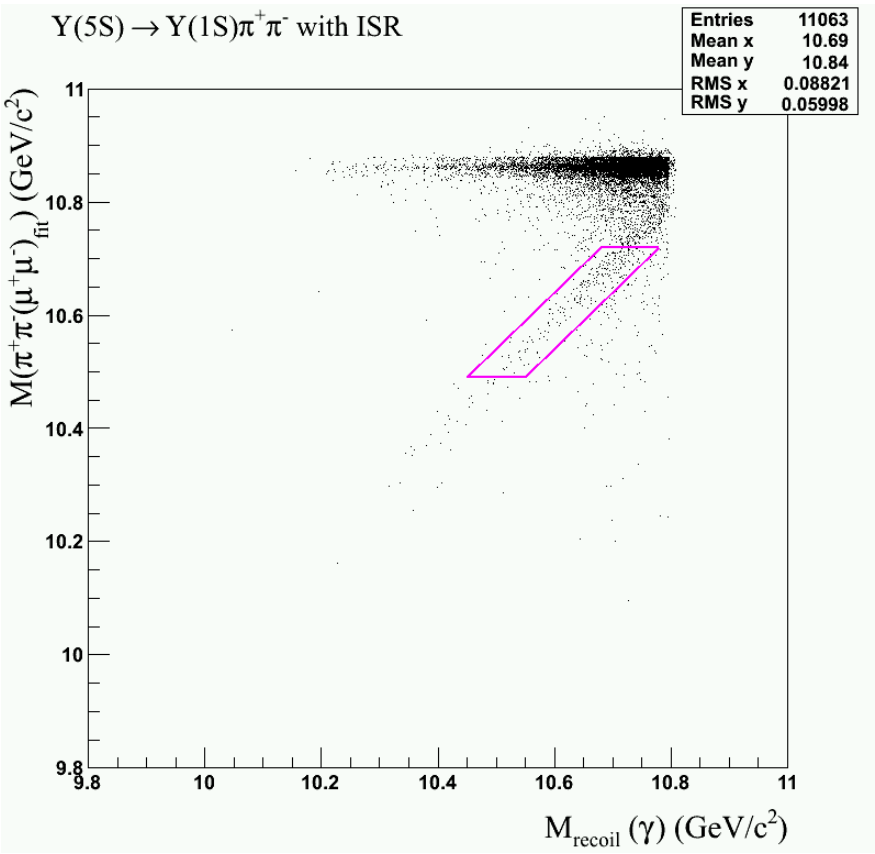

Figure 16: A 2-dimensional $M(\pi^+\pi^-(\mu^+\mu^-)_{\rm fit})$ vs $M_{\rm rec}(\gamma)$ distribution for $\Upsilon(5S) \to \Upsilon(1S)\pi^+\pi^-$ events with ISR (after reweighting). The signal region is outlined in magenta.

6.2.3 Regarding Models Used in ISR Monte Carlo

Figure 16 shows the $M(\pi^+\pi^-(\mu^+\mu^-)_{\rm fit})$ vs $M_{\rm rec}(\gamma)$ distribution for $\Upsilon(5S) \to \Upsilon(1S)\pi^+\pi^-$ events with ISR after running the reweighting procedure. The two plotted variables represent two independent ways to estimate the invariant mass of W_{bJ}, and therefore fully reconstructed events fall along the main diagonal of this plot. When the ISR photon of these backgrounds is selected as the signal photon candidate, these backgrounds are also fully reconstructed and fall along the main diagonal within the signal region. Approximately 3% of reconstructed events fall in the signal region. Fortunately, these backgrounds do not peak in the signal region for the $M(\pi^+\pi^-(\mu^+\mu^-)_{\rm fit})$ distribution.

We simulate $\Upsilon(5S) \to \Upsilon(1S)\pi^+\pi^-$ with ISR using the models listed in Table 7. To determine if the choice of decay models affects the distribution shape of our signal variable

Table 7: Decay models used in Mote Carlo simulation of $\Upsilon(5S) \to \Upsilon(1S)\pi^+\pi^-$ with ISR.

Decay Process	Decay Model used in Mote Carlo Simulation
$\Upsilon(5S) \to \Upsilon(1S)\pi^+\pi^-$	PHSP (generic phase space to n-bodies)
$\Upsilon(1S) \to \mu^+\mu^-$	PHSP (generic phase space to n-bodies)
Initial state radiation	VectorISR ($e^+e^- \to V\gamma$) where V is a vector)
Final state radiation	PHOTOS (modified)

$M(\pi^+\pi^-(\mu^+\mu^-)_{\rm fit})$, we generate additional samples using the VVPIPI decay [20] model for $\Upsilon(5S) \to \Upsilon(1S)\pi^+\pi^-$ and the VLL decay model [20] for $\Upsilon(1S) \to \mu^+\mu^-$. Figure 17 shows the distribution of $M(\pi^+\pi^-(\mu^+\mu^-)_{\rm fit})$ for two different MC samples generated using different decay models. We find that the choice of decay model has only a small effect on the shape of the $M(\pi^+\pi^-(\mu^+\mu^-)_{\rm fit})$ distribution. Furthermore, we plot the $\cos\theta$ of μ^+ in Figure 18 and find that the presence of ISR has only a small effect on the the angular distriubtions of muons. To determine if ISR affects the width of the $M(\pi^+\pi^-(\mu^+\mu^-)_{\rm fit})$ distribution for signal processes $\Upsilon(5S) \to \gamma W_{bJ}$, we generate additional MC samples for the the signal process $\Upsilon(5S) \to \gamma W_{bJ}$ with ISR. We find that ISR has practically no effect on the width of the distribution of $M(\pi^+\pi^-(\mu^+\mu^-)_{\rm fit})$.

6.2.4 Backgrounds with ISR

The dominant source of backgrounds in the signal region is $\Upsilon(5S) \to \Upsilon(1S)\pi^+\pi^-$ with ISR. The rightmost plot in Figure 19 shows the distribution of these events within the signal region for our reweighted MC. We model background of this type using an exponential.

To see how the selection on ΔE affects the background shape, we loosen up the selection on ΔE in the left and middle plots in Figure 19. Imposing a selection on ΔE has only a small effect on the shape of these backgrounds in the signal region.

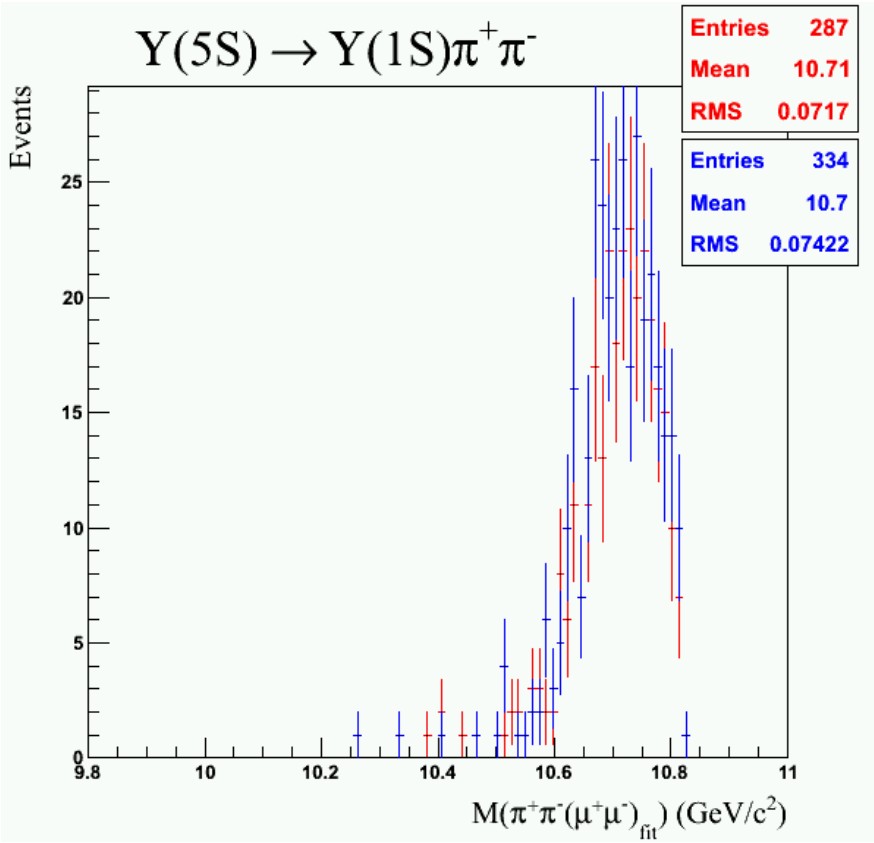

Figure 17: The distribution shown in blue is for events where $\Upsilon(5S) \to \Upsilon(1S)\pi^+\pi^-$ is generated using VVPIPI model [20] and $\Upsilon(1S) \to \mu^+\mu^-$ using VLL model [20]. The distribution shown in red is for events generated using PHSP model [20] for both processes. Neither samples contain ISR nor FSR, so they only differ by their decay models. The shapes of their $M(\pi^+\pi^-(\mu^+\mu^-)_{\rm fit})$ distribution are very similar. Note that although there is a difference in efficiency between the two samples, this is unimportant for our analysis, because we are only interested in possible difference between the shapes of these distributions.

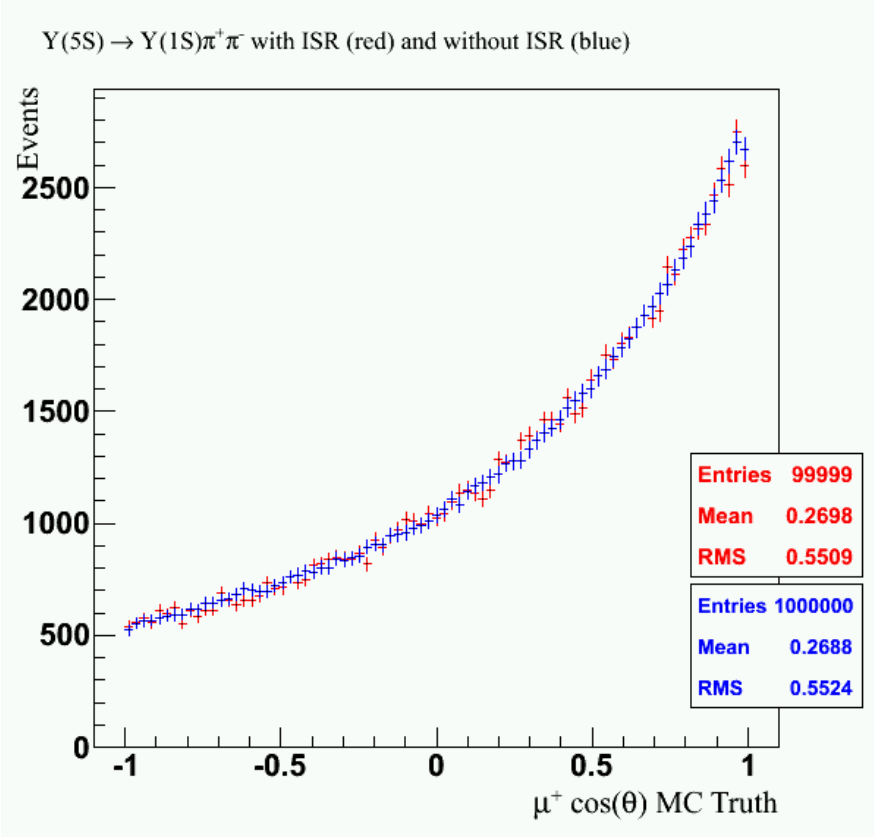

Figure 18: Distributions of $\cos\theta$ for μ^+ for $\Upsilon(5S) \to \Upsilon(1S)\pi^+\pi^-$ events. The distribution shown is red is for events generated with ISR while the distriubtion shown in blue is for events generated without ISR. Events in both distribtuions are generated using PHSP model for both $\Upsilon(5S) \to \Upsilon(1S)\pi^+\pi^-$ and $\Upsilon(1S) \to \mu^+\mu^-$. The blue distribution is normalized to the number of events in the red distribution.

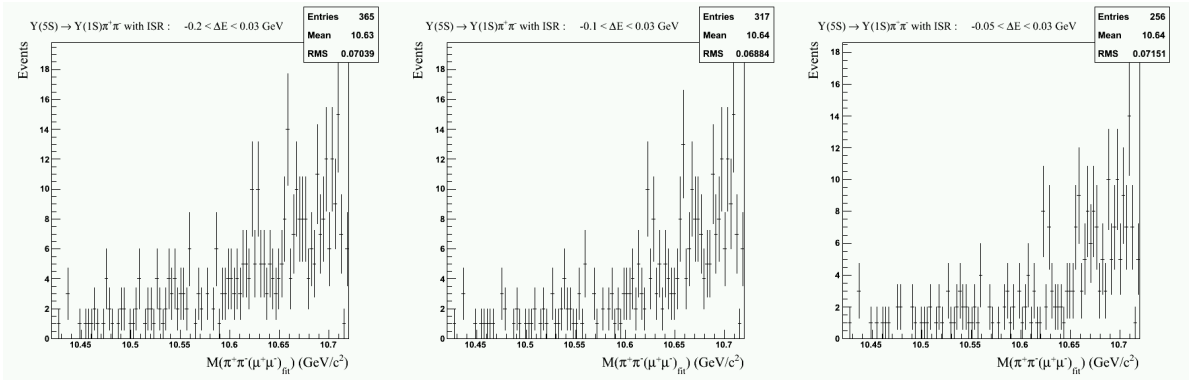

Figure 19: Distributions of $M(\pi^+\pi^-(\mu^+\mu^-)_{\rm fit})$ for $\Upsilon(5S) \to \Upsilon(1S)\pi^+\pi^-$ with ISR in the signal region for different ΔE requirements. The leftmost distribution requires -0.2 GeV $< \Delta E <$ 0.03 GeV, the middle distribution requires -0.1 GeV $< \Delta E <$ 0.03, and the rightmost distribution requires -0.05 GeV $< \Delta E <$ 0.03. The upper bound of ΔE is kept at 0.03 GeV for all distributions, since very few signal events fall beyound $\Delta E >$ 0.03 GeV.

7.0 Fitting

7.1 Signal and Background PDFs

To extract signal yield, we perform a one-dimensional extended unbinned ML fit to the variable $M(\pi^+\pi^-(\mu^+\mu^-)_{\rm fit})$ using RooFit [17]. To simulate beam energy smearing we model the signal distribution of $M(\pi^+\pi^-(\mu^+\mu^-)_{\rm fit})$ using the convolution of a Breit-Wigner with a Gaussian. The observed width and shape of $M(\pi^+\pi^-(\mu^+\mu^-)_{\rm fit})$ distribution in signal MC remains practically the same after applying our ΔE requirement. Including ISR does not have much effect on the observed width either. Therefore, we fix the width of our signal PDF. We set the width of the Gaussian used in convolution to be $\sigma_G = 6$ MeV to match the beam energy resolution. We set the width of the Breit-Wigner to be $\sigma_B = 15$ MeV to match the intrinsic width of Z_b and Z_b'. We let mean of the signal float within the fit, as W_{bJ} could be observed at different invariant masses for different spins J. We use an exponential to model

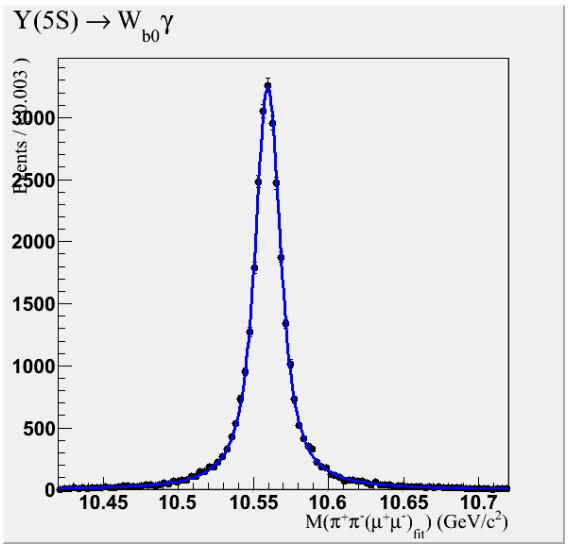

(a) Fit result for the distribution of $M(\pi^+\pi^-(\mu^+\mu^-)_{\rm fit})$ in W_{b0} signal MC

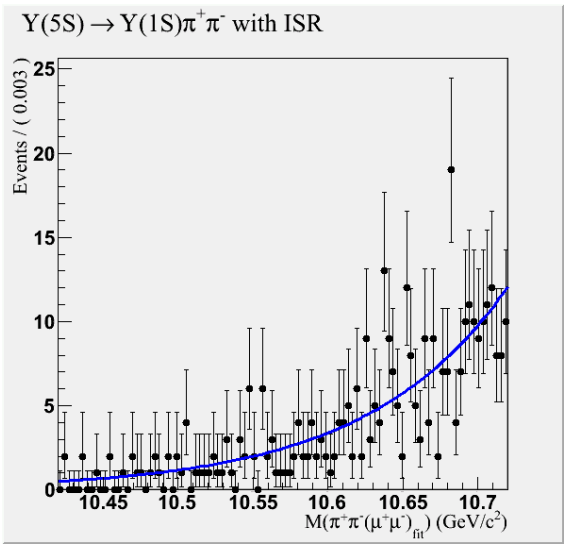

(b) Fit result for the distribution of $M(\pi^+\pi^-(\mu^+\mu^-)_{\rm fit})$ for $\Upsilon(5S) \to \Upsilon(1S)\pi^+\pi^-$ with ISR

Figure 20: Fitting signal and background MC

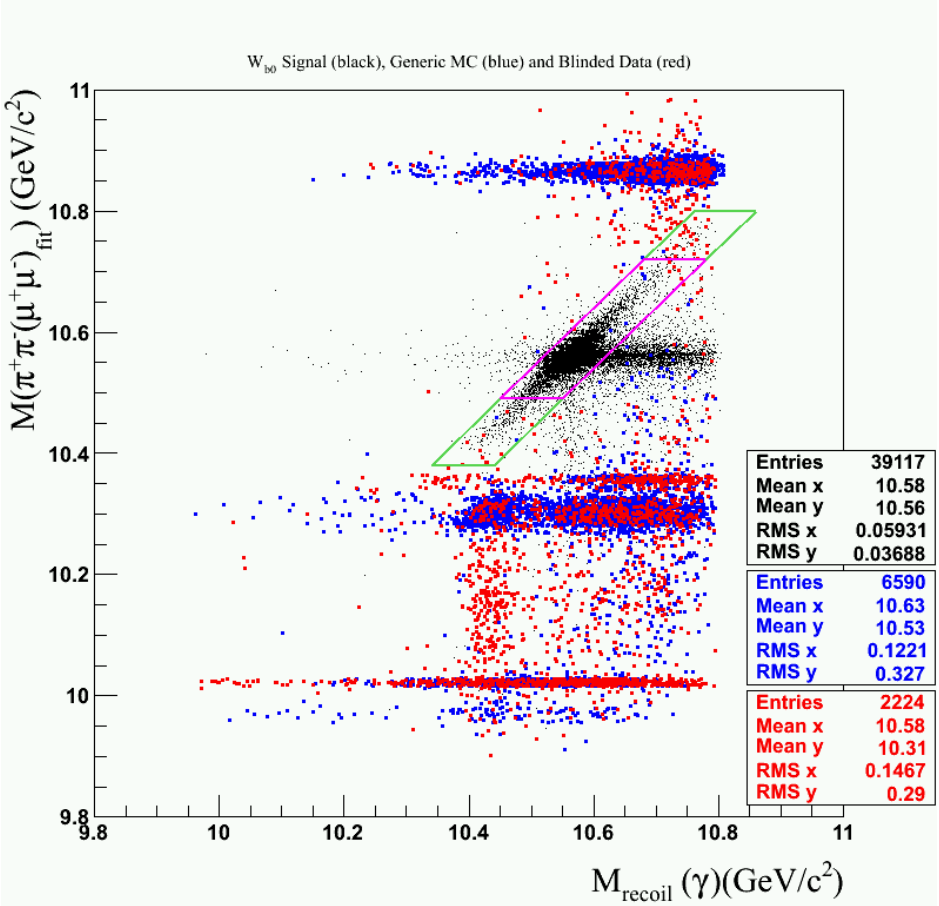

Figure 21: Definition of sideband regions outlined in green. The signal region is shown in magenta.

background contributions due to ISR as well as possible non-resonant contribution from dimuon continuum events. The resulting fits to W_{b0} signal MC and $\Upsilon(5S) \to \Upsilon(1S)\pi^+\pi^-$ MC with ISR are shown in Figure 20.

7.2 Expected Background

To estimate the number of background events we expect in the signal region, we perform an extended unbinned maximum likelihood fit to data only in the sideband regions shown in Figure 21. The sideband regions are defined as the regions within $10.38\,\mathrm{GeV/c^2} \leq$

$M(\pi^+\pi^-(\mu^+\mu^-)_{\rm fit}) \leq 10.49\,{\rm GeV/c^2}$ and $10.72\,{\rm GeV/c^2} \leq M(\pi^+\pi^-(\mu^+\mu^-)_{\rm fit}) \leq 10.80\,{\rm GeV/c^2}$ satisfying $-0.05\,({\rm GeV}) \leq \Delta E \leq 0.05\,{\rm GeV}$. To determine what fraction $F_{\rm sidebands}$ of the fit lies in the sidebands, We integrate the fit over the sidebands and normalize the resulting integral. We find that $F_{\rm sidebands} = 0.46$. We then estimate the number of background events in the signal region as

$$N_{\rm estimate} = N_{\rm data}\frac{1 - F_{\rm sidebands}}{F_{\rm sidebands}} \tag{7.1}$$

where $N_{\rm data}$ is the number of data events in the sideband regions. We have $N_{\rm data} = 27$. Using this approximation, we expect 32 ± 6 background events within the signal region. To account for uncertainty in the number of data events in the sideband region, we fit $M(\pi^+\pi^-(\mu^+\mu^-)_{\rm fit})$ within the range of 10.38 GeV/c^2 and 10.80 GeV/c^2 when extracting signal yield. This range corresponds to the signal region and sideband regions combined. We expect 59 ± 11 background events within the combined signal and sideband region in the full Belle data sample.

7.3 Confidence Belts

To construct a 90% confidence belt, we perform ensemble tests. Each ensemble test consists of 1000 toy MC experiments. In each toy MC experiment, we generate $N_{\rm sig}$ signal events and $N_{\rm bkg}$ background events according to their respective PDF lineshapes used for fitting signal and background. We then fit the generated events in the range $10.38\ {\rm GeV/c^2} < M(\pi^+\pi^-(\mu^+\mu^-)_{\rm fit}) < 10.80\ {\rm GeV/c^2}$ to our combined signal and background PDF to extract the fitted number of signal events $N_{\rm sig}^{\rm fit}$.

We construct our 90% confidence belt by performing ensemble tests with $N_{\rm bkg}^{\rm gen} = 59$ for values of $N_{\rm sig}^{\rm gen}$ from 0 to 70. We additionally construct a 90% confidence belt where we allow Poisson fluctuation in $N_{\rm bkg}^{\rm gen}$. These confidence belts are shown in Figure 22. The lower bound of the belt for a given $N_{\rm sig}^{\rm gen}$ corresponds to the value at which 5% of ensemble tests yield a value of $N_{\rm sig}^{\rm fit}$ less than this value. Simlarly, the upper bound of the belt for a given $N_{\rm sig}^{\rm gen}$ corresponds to the value at which 5% of ensemble tests yield a value of $N_{\rm sig}^{\rm fit}$ greater than this value.

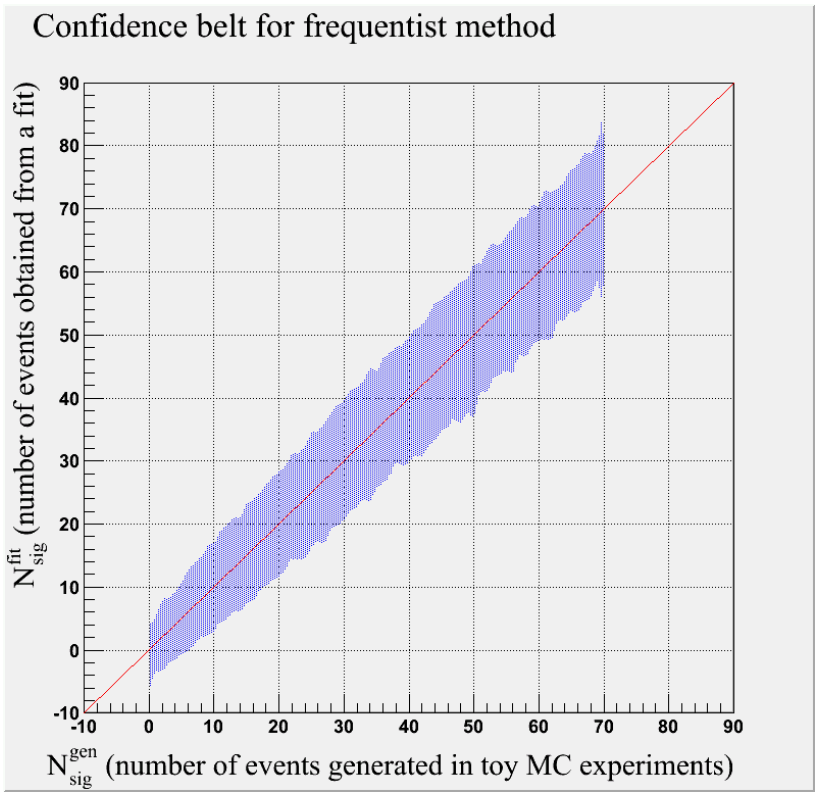

(a) Does not include Poisson fluctuations in $N_{\mathrm{bkg}}^{\mathrm{gen}}$

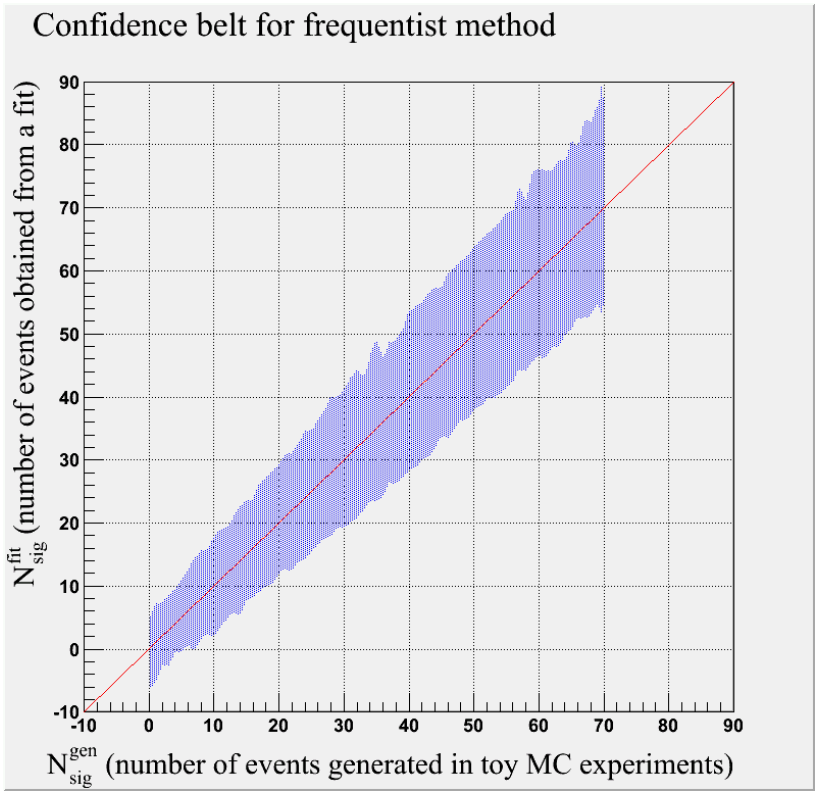

(b) Includes Poisson fluctuations in $N_{\mathrm{bkg}}^{\mathrm{gen}}$.

Figure 22: 90% confidence belts for frequentist method.

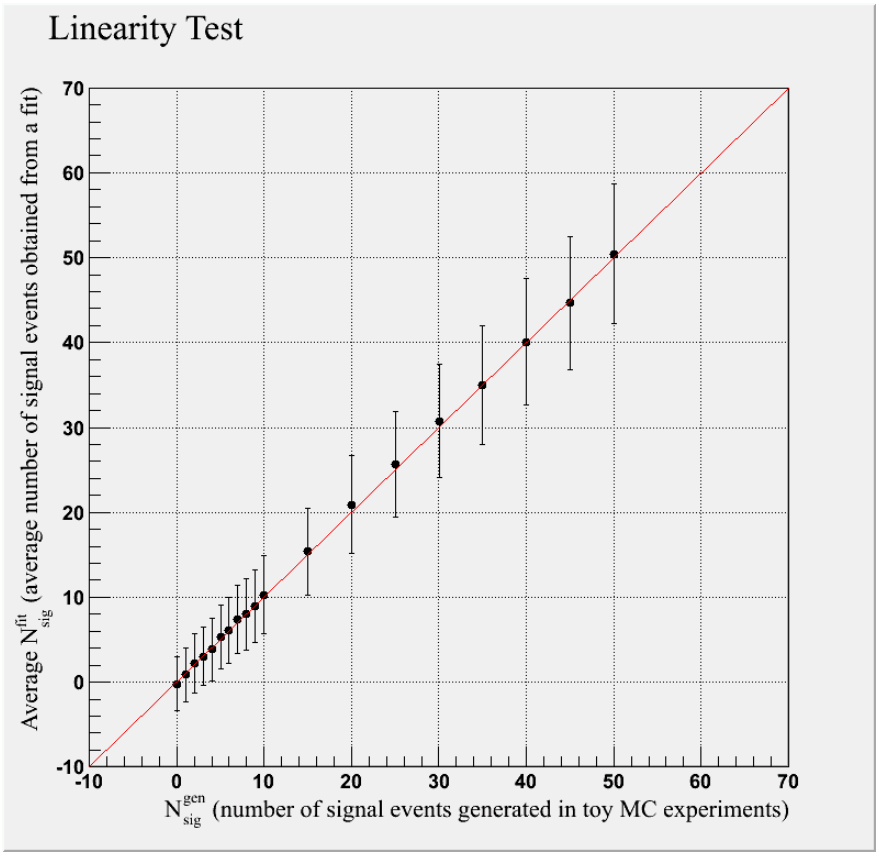

Figure 23: Average $N_{\text{sig}}^{\text{fit}}$ for varying values of $N_{\text{sig}}^{\text{gen}}$.

7.4 Linearity Study

To validate our fitting procedures, we perform a linearity study using ensemble tests. Ensemble tests are generated as described in Section 7.3. For each ensemble test of 1000 toy MC experiments, we calculate the average number of signal events from the fit and the error associated with the average. We vary $N_{\text{sig}}^{\text{gen}}$ from 0 to 10 in steps of 1 and from 10 to 50 in steps of 5 while fixing $N_{\text{bkg}} = 59$.

We plot the average number of signal events from the fit against $N_{\text{sig}}^{\text{gen}}$ as shown in Figure 23. Figure 24 displays distriubtions of $N_{\text{sig}}^{\text{fit}}$ for certain values of $N_{\text{sig}}^{\text{gen}}$. We find that the for large values of $N_{\text{sig}}^{\text{gen}}$, the distribution of $N_{\text{sig}}^{\text{fit}}$ is unbiased. For small values of $N_{\text{sig}}^{\text{gen}}$, the distribution of $N_{\text{sig}}^{\text{fit}}$ is asymmetric, indicating a small bias.

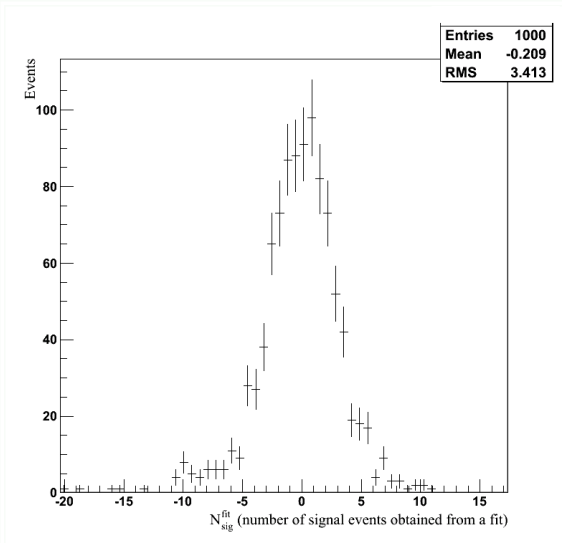

(a) Distribution of $N_{\rm sig}^{\rm fit}$ for an ensemble test with $N_{\rm sig}^{\rm gen} = 0$ and $N_{\rm bkg}^{\rm gen} = 59$.

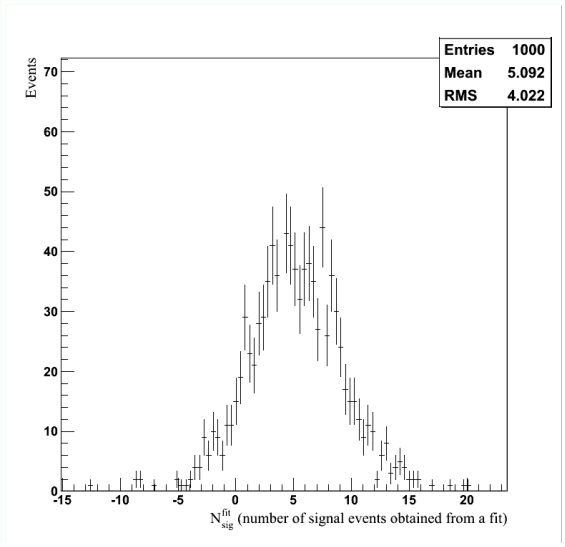

(b) Distribution of $N_{\rm sig}^{\rm fit}$ for an ensemble test with $N_{\rm sig}^{\rm gen} = 5$ and $N_{\rm bkg}^{\rm gen} = 59$.

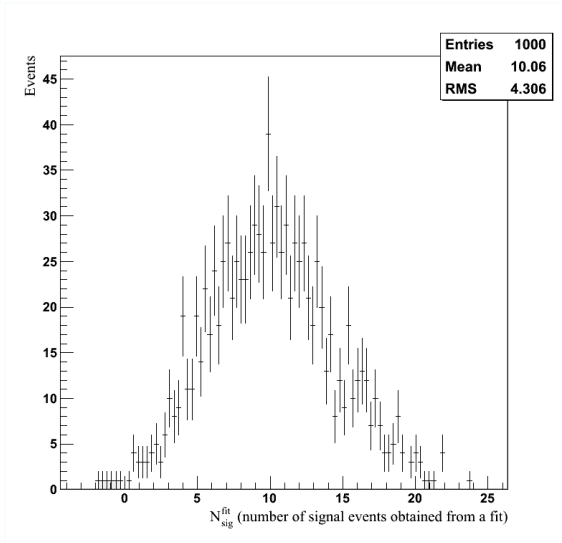

(c) Distribution of $N_{\rm sig}^{\rm fit}$ for an ensemble test with $N_{\rm sig}^{\rm gen} = 10$ and $N_{\rm bkg}^{\rm gen} = 59$.

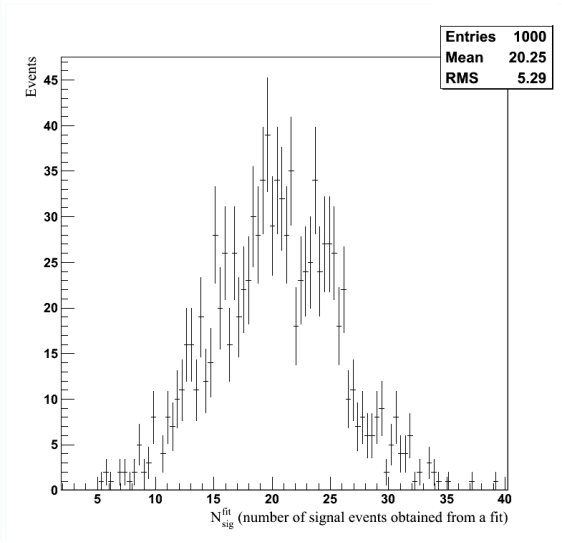

(d) Distribution of $N_{\rm sig}^{\rm fit}$ for an ensemble test with $N_{\rm sig}^{\rm gen} = 20$ and $N_{\rm bkg}^{\rm gen} = 59$.

Figure 24: $N_{\rm sig}^{\rm fit}$ Distributions for ensemble tests with different $N_{\rm sig}^{\rm gen}$.

7.5 Sensitivity Estimation

We estimate the upper limit on the branching fraction of $\Upsilon(5S) \to \gamma W_{bJ}$ in the absence of signal by performing a maximum likelihood fit on toy MC generated according to the fit

Table 8: Values used to calculate upper limit on the branching fraction. Uncertainty in $\mathcal{B}(\rho^0 \to \pi^+\pi^-)$ is negligible.

Quanitity	Value
$N_{\rm sig}$	0.2 ± 3.2
ϵ	$(29 \pm 0.17)\%$
$N_{\Upsilon(5S)}$	$(6.53 \pm 0.66) \cdot 10^6$
$\mathcal{B}(\Upsilon(1S) \to \mu^+\mu^-)$	$(2.48 \pm 0.05)\%$
$\mathcal{B}(\rho^0 \to \pi^+\pi^-)$	99.8%

to the data sidebands. We generate 1000 toy MC samples with 59 background events, fit our combined signal and background shape to each sample, and then average the resulting signal yields. There is an average signal yield of -0.2 ± 3.2 events. Note that in Figure 23, this average signal yield corresponds to the value plotted at $N_{\rm sig}^{\rm gen} = 0$. Using the confidence belt in Figure 22, we determine the upper limit on the number of signal events to be 10 events. We calculate the upper limit on the branching fraction in the absence of signal as follows:

$$\mathcal{B}(\Upsilon(5S) \to \gamma W_{bJ}) \cdot \mathcal{B}(W_{bJ} \to \Upsilon(1S)\rho^0) = \frac{N_{\rm sig}}{\epsilon \cdot N_{\Upsilon(5S)} \cdot \mathcal{B}(\Upsilon(1S) \to \mu^+\mu^-) \cdot \mathcal{B}(\rho^0 \to \pi^+\pi^-)} \tag{7.2}$$

where $N_{\Upsilon(5S)}$ is the number of $\Upsilon(5S)$ and ϵ is our reconstruction efficiency. Using Eq. 7.2, we determine the upper limit on the bracnhing fraction in the absence of signal to be $2.4 \cdot 10^{-4}$. All values used to calcuate the branching fraction are shown in Table 8.

8.0 Outlook

In this analysis, we search for a new molecular state W_{bJ} produced in the radiative transition $\Upsilon(5S) \to \gamma W_{bJ}$ followed by the decays $W_{bJ} \to \Upsilon(1S)\rho^0$, $\Upsilon(1S) \to \mu^+\mu^-$, $\rho^0 \to \pi^+\pi^-$ We fully reconstruct the signal final state consisting of two muons, two pions, and a photon We perform a blind analysis by optimizing our selection criteria and analysis techniques using only MC samples before applying them to data. To search for the presence of W_{bJ} in Belle data, we will "unblind" 15% of the data in the signal region and then fit a one-dimensional distribution of $M(\pi^+\pi^-(\mu^+\mu^-)_{\rm fit})$ using the aforementioned models for signal and background shapes. We will use our confidence belt (Figure 22) to either claim a discovery of W_{bJ} or establish an upper limit on the signal production rate (branching fraction) for the radiative decay $\Upsilon(5S) \to \gamma W_{bJ}$. The following sources of systematic uncertainties will be considered in our final estimate of the upper limit of the branching fraction of $\Upsilon(5S) \to \gamma W_{bJ}$:

- Number of $B_s^{(*)}\bar{B}_s{}^{(*)}$ pairs
- Signal Reconstruction Efficiency
- Daughter Branching Fractions
- MC statistics
- PDF parameterization
- Fit bias
- Fraction of contributions from $B_s^*\bar{B}_s^*$, $B_s^*\bar{B}_s$, and $B_s\bar{B}_s$
- Trigger efficiency

As mentioned in 1.1.3, W_{bJ} can also be produced in hadronic transitions from $\Upsilon(5,6S)$ with the emission of a ρ meson rather than a photon. However, this process is suppressed by phase space at $\Upsilon(5S)$; after the transition to W_{bJ}, there would not be enough energy left for the pion pair in the tail of the ρ invariant mass. For this reason, we have to allow for $q\bar{q}$ to produce the radiative photon instead, thus suppressing the production rate for this decay by a factor of $\alpha \approx \frac{1}{137}$.

Although statistics are limited in current Belle data, in near future, the Belle II experiment will run at an instantaneous luminosity 40 times larger than that of the original Belle experiment, potentially improving prospects of a W_{bJ} discovery. Belle II additionally aims to accumulate data at $\Upsilon(6S)$ resonance center-of-mass energy, allowing for the future study of hadronic transitions to W_{bJ} as well as additional studies to understand the Z_b states.

9.0 Appendix

9.1 Final State Radiation

In the version of package PHOTOS used by Belle, the minimum FSR photon energy (evaluated in the center of mass frame of charged particle's parent) is calculated as follows:

$$E(\gamma_{FSR}) = (\text{XPHCUT}) \cdot 0.5 \cdot M(\text{parent}) \tag{9.1}$$

where XPHCUT is a hardcoded constant set to 0.01. Hence, the minimum FSR energy is approximately 4 MeV for pions ($M(\rho^0) = 770$ MeV) and 50 MeV for muons ($M(\Upsilon(1S)) = 9.46$ GeV). The lower limit on FSR energy for muons is too high, so we lowered the value of XPHCUT to 10^{-7}. To accomplish this, we changed XPHCUT=0.01D0 to XPHCUT=0.0000001D0, recompiled the phocin.F source code and then rebuilt EvtGen with an updated PHOTOS library.

To verify that XPHCUT was successfully lowered to 10^{-7}, we plot the ratios $\frac{E(\gamma_{FSR})}{M(\Upsilon(1S))}$

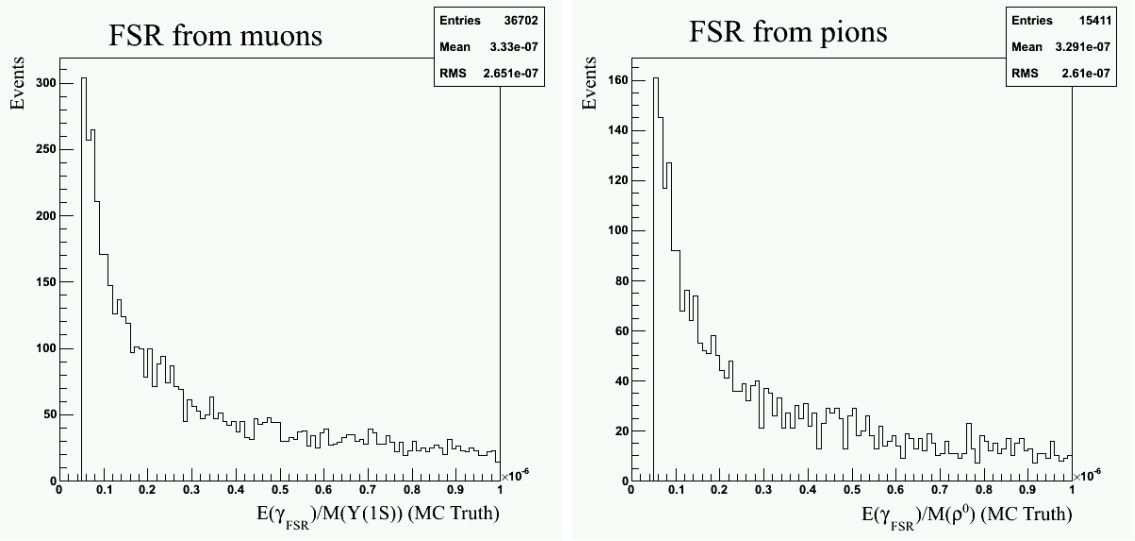

(a) FSR from muons.

(b) FSR from pions.

Figure 25: Final state radiation from charged tracks

and $\frac{E(\gamma^{\rho}_{FSR})}{M(\rho)}$ as generated in Figure 25. Because these quantities are bounded from below by XPHCUT $\cdot$ 0.5, we prove that XPHCUT was successfully lowered.

Bibliography

[1] A. Bondar et al. Observation of two charged bottomonium-like resonances in Y(5S) decays. *Phys. Rev. Lett.*, 108:122001, 2012.

[2] I. Adachi et al. Evidence for a $Z_b^0(10610)$ in Dalitz analysis of $\Upsilon(5S) \to Y(nS)\pi^0\pi^0$. 2012.

[3] P. Krokovny et al. First observation of the $Z_b^0(10610)$ in a Dalitz analysis of $\Upsilon(10860)$ $\to \Upsilon(\mathrm{nS})\pi^0\pi^0$. *Phys. Rev.*, D88(5):052016, 2013.

[4] A. Garmash et al. Observation of $Z_b(10610)$ and $Z_b(10650)$ Decaying to B Mesons. *Phys. Rev. Lett.*, 116(21):212001, 2016.

[5] L. M. Lederman. The discovery of the Upsilon, bottom quark, and B mesons. In *The Rise of the standard model: Particle physics in the 1960s and 1970s. Proceedings, Conference, Stanford, USA, June 24-27, 1992*, pages 101–113, 1992.

[6] M. Tanabashi et al. Review of Particle Physics. *Phys. Rev.*, D98(3):030001, 2018.

[7] S. Godfrey and N. Isgur. Mesons in a Relativized Quark Model with Chromodynamics. *Phys. Rev.*, D32:189–231, 1985.

[8] S. Godfrey and K. Moats. Bottomonium Mesons and Strategies for their Observation. *Phys. Rev.*, D92(5):054034, 2015.

[9] S. Godfrey, K. Moats, and E. S. Swanson. B and B_s Meson Spectroscopy. *Phys. Rev.*, D94(5):054025, 2016.

[10] A. E. Bondar, R. V. Mizuk, and M. B. Voloshin. Bottomonium-like states: Physics case for energy scan above the $B\bar{B}$ threshold at Belle-II. *Mod. Phys. Lett.*, A32(04):1750025, 2017.

[11] A. E. Bondar, A. Garmash, A. I. Milstein, R. Mizuk, and M. B. Voloshin. Heavy quark spin structure in Z_b resonances. *Phys. Rev.*, D84:054010, 2011.

[12] Stephen Lars Olsen. A New Hadron Spectroscopy. *Front. Phys.(Beijing)*, 10(2):121–154, 2015.

[13] M. B. Voloshin. Radiative transitions from Upsilon(5S) to molecular bottomonium. *Phys. Rev.*, D84:031502, 2011.

[14] W. Altmannshofer et al. The Belle II Physics Book. 2018.

[15] S. Kurokawa and E. Kikutani. Overview of the KEKB accelerators. *Nuclear Instruments and Methods A*, 499(1):1 – 7, 2003.

[16] A. Abashian et. al. (Belle Collaboration). The Belle Detector. *Nuclear Instruments and Methods A*, 479(1):117 – 232, 2002.

[17] Wouter Verkerke and David P. Kirkby. The RooFit toolkit for data modeling. *eConf*, C0303241:MOLT007, 2003. [186(2003)].

[18] D. J. Lange. The EvtGen particle decay simulation package. *Nucl. Instrum. Meth.*, A462:152–155, 2001.

[19] S. Agostinelli et al. GEANT4: A Simulation toolkit. *Nucl. Instrum. Meth.*, A506:250–303, 2003.

[20] A. Ryd, D. Lange, N. Kuznetsova, S. Versille, M. Rotondo, D. P. Kirkby, F. K. Wuerthwein, and A. Ishikawa. EvtGen: A Monte Carlo Generator for B-Physics. 2005.

[21] E. Barberio and Z. Was. PHOTOS: A Universal Monte Carlo for QED radiative corrections. Version 2.0. *Comput. Phys. Commun.*, 79:291–308, 1994.

[22] J. Brodzicka et al. Physics Achievements from the Belle Experiment. *PTEP*, 2012:04D001, 2012.

[23] M. Tanabashi et al. Review of particle physics. *Phys. Rev. D*, 98:030001, Aug 2018.

[24] M. Benayoun, S. I. Eidelman, V. N. Ivanchenko, and Z. K. Silagadze. Spectroscopy at B factories using hard photon emission. *Mod. Phys. Lett.*, A14:2605–2614, 1999. [Frascati Phys. Ser.15(1999)].